SCIENCE CHINA
Information Sciences

• REVIEW •
Special Focus on Quantum Information

October 2022, Vol. 65 200501:1–200501:19
https://doi.org/10.1007/s11432-022-3550-1

Review of noble-gas spin amplification via the spin-exchange collisions

Haowen SU[1,2], Min JIANG[1,2*] & Xinhua PENG[1,2*]

[1]*CAS Key Laboratory of Microscale Magnetic Resonance and School of Physical Sciences, University of Science and Technology of China, Hefei 230026, China;*
[2]*CAS Center for Excellence in Quantum Information and Quantum Physics, University of Science and Technology of China, Hefei 230026, China*

Received 21 June 2022/Accepted 12 July 2022/Published online 30 August 2022

Abstract Due to isolation from the environment with the protection of the full electronic shells, nuclear spins of noble gas typically feature extraordinary long coherence times, high polarization and good chemical inertness, which makes themselves attractive in extensive scientific applications. Recently, the noble-gas spin amplification via the spin-exchange collisions between overlapping noble-gas spins and alkali-atom spins has been theoretically and experimentally demonstrated in various quantum techniques including maser, Floquet maser, spin-based amplifier, and Floquet spin amplifier. The noble-gas spin amplification can enhance the external oscillating magnetic field by a factor of more than 100 and realize ultrasensitive magnetometry, which is important for the detection of weak electromagnetic fields and hypothetical particles. Based on the spin amplification, experiments have been conducted to search for axion-like dark matter and exotic spin-dependent forces and new constraints have been established. This review summarizes the recent progress on noble-gas spin amplification, including the basic principles, methods, different types, the related applications ranging from magnetic-field sensing to searches for new physics, and prospects for further improvements.

Keywords nuclear spin, noble gas, maser, spin amplification, Floquet system

Citation Su H W, Jiang M, Peng X H. Review of noble-gas spin amplification via the spin-exchange collisions. Sci China Inf Sci, 2022, 65(10): 200501, https://doi.org/10.1007/s11432-022-3550-1

1 Introduction

Noble-gas science came to life one century ago and has been expanding ever since. The discovery and studies of noble gas were recognized in 1904 by the Nobel Prize in Chemistry. Following the theory of nuclear spins recognized by Nobel Prize in Physics in 1933 [1], noble-gas isotopes (e.g., Helium-3, Neon-21, and Xeon-129) were found with non-zero nuclear spin. These isotopes show outstanding features and stimulate extensive scientific applications. First, noble gas has good chemical inertness and thus can overlap with other atomic or molecular gas (such as alkali-metal vapor) and even can be inhaled into human lungs [2, 3]. The chemical inertness of noble gas provides the prerequisite to functioning as a probe of other systems and surface interactions [4]. Second, noble-gas nuclear spins can be highly polarized to close to 100% using spin-exchange (SEOP) and metastability-exchange (MEOP) optical pumping [2, 5]. Highly-polarized noble gas enables one to obtain a large signal-to-noise ratio in precision measurements, such as magnetic field sensing [6–10], atomic gyroscope [11], and realizing the highest resolution imaging of human air spaces [3]. Third, nuclear spins of noble gas can maintain coherence for hours, because they are well isolated from the environment with the protection of the full electronic shells. Long-lived coherence makes polarized noble gas extremely stable and sensitive for precision measurements [12]. These outstanding features provide a variety of concrete applications, ranging from magnetic resonance imaging [10], magnetic field sensing [2, 5], inertial rotation sensing [11], and quantum information science [13–15] to searches for new physics beyond the standard model [16–23].

* Corresponding author (email: dxjm@ustc.edu.cn, xhpeng@ustc.edu.cn)

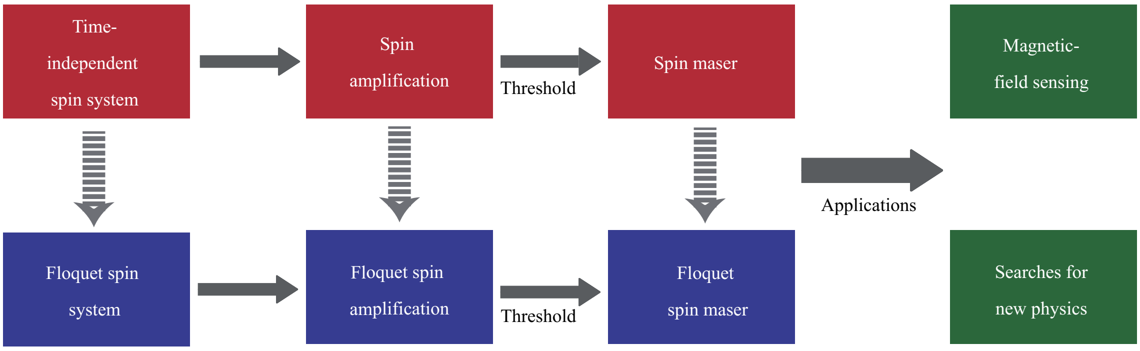

Figure 1 (Color online) Schematics of the recent progress of the spin amplification techniques in a hybrid vapor cell of noble gas and alkali-metal atoms. The spin amplification techniques are developed on two kinds of different physical models. (i) The time-independent spin systems without a periodically driven field, and (ii) Floquet spin systems with a periodically driving field. Then, the corresponding technique including spin amplification and maser is demonstrated in these two systems. Finally, various applications including magnetic-field sensing and searches for new physics are demonstrated.

In this brief review, we focus on the recent development of noble-gas spin amplification, which is the key to the recently demonstrated maser, Floquet maser [17], spin-based amplifier [16], Floquet spin amplifier [24], and their applications in precision measurements [18, 19]. As shown in Figure 1, we first introduce physical systems used in noble-gas spin amplification, such as overlapping ensembles of noble gas and alkali-metal atoms without or with a periodically driving field. Coupled Bloch equations are used to describe the spin dynamics of such physical systems. Subsequently, the basic principles of noble-gas spin amplification and Floquet spin amplification are presented. Based on such amplification effects, a variety of noble-gas spin sensors can be realized, such as maser and Floquet maser. Ultrasensitive magnetometry and searches for new physics are introduced using these spin sensors. Finally, we outline the future prospects of noble-gas spin amplification in further improvement, fundamental physics, etc.

2 Noble-gas spin systems

Figure 2 shows a typical experimental arrangement for noble-gas (e.g., ^{129}Xe-^{87}Rb) spin system demonstrated in [16–19, 24]. A glass cell of a few cm^3 volume contains the gases of interest, namely, alkali-metal vapor and a noble gas, plus nitrogen. The cell is magnetically shielded and heated at a constant temperature to ensure an adequate saturated vapor pressure (typically 10^{11}–10^{14} cm^3) from a few droplets of alkali metal (several milligrams) in the cell. Two sets of three pairs of orthogonal coils are placed around the vapor cell to provide bias and oscillating magnetic fields in an arbitrary direction. A bias field B_z^0 is applied along z to tune the noble-gas Larmor frequency. A circularly polarized pump beam along z polarizes the alkali-metal electron spins. The noble-gas nuclear spins are polarized through the spin-exchange collisions with polarized electron spins. The electron spin polarization $P_x^{\rm e}$ of alkali-metal atoms along x is detected through the optical rotation of a linearly polarized probe beam along x (see [25–27]):

$$\theta = \frac{1}{4} l r_{\rm e} {\rm c} f n P_x^{\rm e} D(V), \tag{1}$$

where l is the optical path length, $r_{\rm e}$ is the classical radius of the electron, c is the speed of light, f is the oscillator strength, n is the ^{87}Rb atomic density, $D(V) = (V - V_0)/[(V - V_0)^2 + (\Delta V/2)^2]$, V is the frequency of the probe beam, and ΔV is the full-width at half-maximum (FWHM) of the optical transition of frequency V_0.

In the vapor cell, the alkali-metal spins spatially overlap with the noble-gas spins. The spin dynamics of these two spins can be described by the coupled Bloch equations [16, 18, 19]:

$$\frac{\partial \boldsymbol{P}^{\rm e}}{\partial t} = \frac{\gamma_{\rm e}}{Q}(B_z^0 \hat{z} + \boldsymbol{B}_a + \beta M_0^{\rm n} \boldsymbol{P}^{\rm n}) \times \boldsymbol{P}^{\rm e} + \frac{P_0^{\rm e} \hat{z} - \boldsymbol{P}^{\rm e}}{\{T_{2\rm e}, T_{2\rm e}, T_{1\rm e}\} Q}, \tag{2}$$

$$\frac{\partial \boldsymbol{P}^{\rm n}}{\partial t} = \gamma_{\rm n}(B_z^0 \hat{z} + \boldsymbol{B}_a + \beta M_0^{\rm e} \boldsymbol{P}^{\rm e}) \times \boldsymbol{P}^{\rm n} + \frac{P_0^{\rm n} \hat{z} - \boldsymbol{P}^{\rm n}}{\{T_{2\rm n}, T_{2\rm n}, T_{1\rm n}\}}, \tag{3}$$

where $\boldsymbol{P}^{\rm e}$ ($\boldsymbol{P}^{\rm n}$) is the polarization of alkali-metal electrons (noble-gas nuclei), $\gamma_{\rm e}$ ($\gamma_{\rm n}$) is the gyromagnetic ratio of a bare electron (noble-gas nuclei), $\boldsymbol{B}_a$ is the external oscillating magnetic field, $M_0^{\rm e}$ ($M_0^{\rm n}$) is the magnetization of alkali-metal (noble-gas) spins with unity polarization, $T_{1\mathrm{n}}$ ($T_{2\mathrm{n}}$) is the longitudinal (transverse) relaxation time of noble-gas spins, and $T_{1\mathrm{e}}$ ($T_{2\mathrm{e}}$) is the longitudinal (transverse) relaxation times of alkali-metal spins. T_{e} ($T_{1\mathrm{e}} \approx T_{2\mathrm{e}}$) can be regarded as the common relaxation time without distinction here. The factor Q is the slowing-down factor of alkali-metal atoms depending on the polarization. Because P_z^{e} is much larger than the transverse components P_x^{e} and P_y^{e}, Q primarily depends on $P_z^{\mathrm{e}} \approx P_0^{\mathrm{e}}$. Therefore, Q can be approximated as a constant.

Due to the Fermi-contact interactions between alkali-metal electrons and noble-gas nuclear spins, an effective field $\beta M_0^{\mathrm{e,n}} \boldsymbol{P}^{\mathrm{e,n}}$ is induced by the polarization $\boldsymbol{P}^{\mathrm{e,n}}$, where $\beta = 8\pi\kappa_0/3$ and κ_0 is the Fermi-contact factor. Due to $\beta M_0^{\mathrm{e}} \boldsymbol{P}^{\mathrm{e}} \ll \beta M_0^{\mathrm{n}} \boldsymbol{P}^{\mathrm{n}}$, we thus neglect the $\beta M_0^{\mathrm{e}} \boldsymbol{P}^{\mathrm{e}}$ term. As a result, the coupled Bloch equations in (2) and (3) can be simplified to

$$\frac{\partial \boldsymbol{P}^{\mathrm{e}}}{\partial t} = \frac{\gamma_{\mathrm{e}}}{Q}(B_z^0 \hat{z} + \boldsymbol{B}_a + \beta M_0^{\mathrm{n}} \boldsymbol{P}^{\mathrm{n}}) \times \boldsymbol{P}^{\mathrm{e}} + \frac{P_0^{\mathrm{e}} \hat{z} - \boldsymbol{P}^{\mathrm{e}}}{T_{\mathrm{e}} Q}, \tag{4}$$

$$\frac{\partial \boldsymbol{P}^{\mathrm{n}}}{\partial t} = \gamma_{\mathrm{n}}(B_z^0 \hat{z} + \boldsymbol{B}_a) \times \boldsymbol{P}^{\mathrm{n}} + \frac{P_0^{\mathrm{n}} \hat{z} - \boldsymbol{P}^{\mathrm{n}}}{\{T_{2\mathrm{n}}, T_{2\mathrm{n}}, T_{1\mathrm{n}}\}}. \tag{5}$$

The solution of the coupled Bloch equations (4) and (5) gives the performance of the noble-gas spin system. The evolution of $\boldsymbol{P}^{\mathrm{n}}$ in (5) is independent on $\boldsymbol{P}^{\mathrm{e}}$ and thus can be calculated independently. In the following, we consider the response of noble-gas spins to a weak external oscillating field $\boldsymbol{B}_a = B_a \cos(2\pi\nu t)\hat{y}$ for two cases: without/with a periodically driven alternating current (AC) field parallel to the bias field, i.e., along z axis (see details in [16, 18, 19, 24]).

2.1 Spin dynamics without a periodically driving field

We first solve the evolution of noble-gas nuclear spins under a bias field B_z^0 along z and an oscillating magnetic field $\boldsymbol{B}_a = B_a \cos(2\pi\nu t)\hat{y}$ from (5). With rotating-wave approximation and $\boldsymbol{B}_{\mathrm{eff}}^{\mathrm{n}} = \beta M_0^{\mathrm{n}} \boldsymbol{P}^{\mathrm{n}}$, we can derive the steady-state effective field experienced by alkali-metal atoms as [16, 18, 19, 24]

$$\boldsymbol{B}_{\mathrm{eff}}^{\mathrm{n}} = \frac{1}{2}\beta M_0^{\mathrm{n}} P_0^{\mathrm{n}} \gamma_{\mathrm{n}} B_a \left\{ \frac{T_{2\mathrm{n}} \cos(2\pi\nu t) + 2\pi\delta\nu T_{2\mathrm{n}}^2 \sin(2\pi\nu t)}{1 + (\gamma_{\mathrm{n}} B_a/2)^2 T_{1\mathrm{n}} T_{2\mathrm{n}} + (2\pi\delta\nu)^2 T_{2\mathrm{n}}^2} \hat{x} + \frac{T_{2\mathrm{n}} \sin(2\pi\nu t) - 2\pi\delta\nu T_{2\mathrm{n}}^2 \cos(2\pi\nu t)}{1 + (\gamma_{\mathrm{n}} B_a/2)^2 T_{1\mathrm{n}} T_{2\mathrm{n}} + (2\pi\delta\nu)^2 T_{2\mathrm{n}}^2} \hat{y} \right\}, \tag{6}$$

where $\delta\nu = \nu - \nu_0$ is the detuning of the external oscillating field with respect to the Larmor frequency of noble-gas nuclear spins $\nu_0 = \gamma_{\mathrm{n}} B_z^0/(2\pi)$. The total magnetic field $\boldsymbol{B}_{\mathrm{tot}}$ on ^{87}Rb detected can be written as

$$\boldsymbol{B}_{\mathrm{tot}} = \boldsymbol{B}_{\mathrm{eff}}^{\mathrm{n}} + B_a \cos(2\pi\nu t)\hat{y}. \tag{7}$$

The alkali-metal spins actually experience the superposition of these two fields.

We now solve for the evolution of alkali-metal spins from (4). In the experimental configuration, the x component of alkali-metal polarization P_x^{e} is detected with a probe beam (see (1)). Thus, we only need to obtain the explicit expression of P_x^{e}. Under the quasi-static field condition, we can obtain the steady-state solution:

$$P_x^{\mathrm{e}} \propto \frac{B_x B_z - B_y \Delta B}{|\boldsymbol{B}|^2 + (\Delta B)^2} \approx \frac{B_x B_z - B_y \Delta B}{(B_z^0)^2 + (\Delta B)^2}, \tag{8}$$

where $\Delta B = 1/(\gamma_{\mathrm{e}} T_{\mathrm{e}})$ and $\boldsymbol{B} \approx B_z^0$ for the large bias field applied along z. In experiments, the measured B_x and B_y are from the total magnetic field in (7), where the effective field generated by nuclear transverse magnetization in the xy plane is the dominant part [16–18, 24].

Based on (6), the effective field $\boldsymbol{B}_{\mathrm{eff}}^{\mathrm{n}}$ induced by the magnetization of the noble-gas nuclear spins depends on the amplitude of the applied oscillating field $\boldsymbol{B}_a$. There are three different situations.

(1) Linear case. When B_a is weak enough to satisfy the condition $(\gamma_{\mathrm{n}} B_a/2)^2 T_{1\mathrm{n}} T_{2\mathrm{n}} \ll 1$, i.e.,

$$B_a \ll \frac{2}{\gamma_{\mathrm{n}} \sqrt{T_{1\mathrm{n}} T_{2\mathrm{n}}}}, \tag{9}$$

the effective field $\boldsymbol{B}_{\mathrm{eff}}^{\mathrm{n}}$ is proportional to the amplitude of applied oscillating field B_a, as shown in Figure 3(a).

(2) Nonlinear case. When B_a is comparable to $2/(\gamma_n \sqrt{T_{1\mathrm{n}} T_{2\mathrm{n}}})$, the $(\gamma_{\mathrm{n}} B_a/2)^2 T_{1\mathrm{n}} T_{2\mathrm{n}}$ term becomes significant and the response becomes nonlinear, as shown in Figure 3(b).

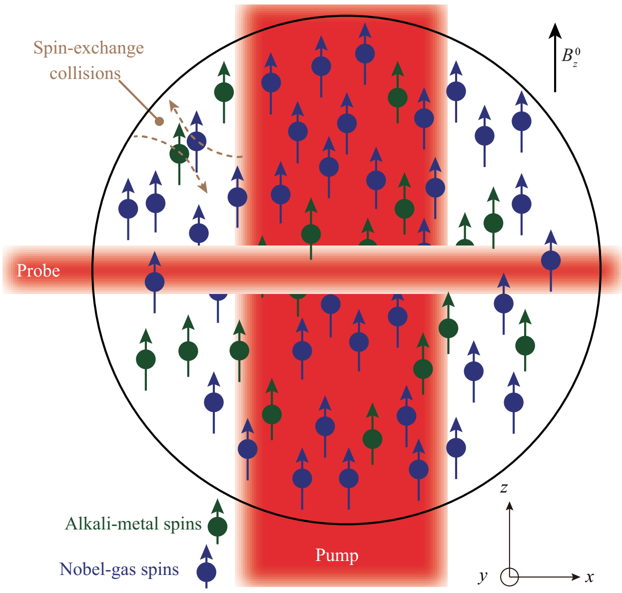

Figure 2 (Color online) Noble-gas spin system. In the noble-gas-alkali-metal vapor cell, the noble-gas nuclear spins (e.g., ^{129}Xe) spatially overlap with the alkali-metal atoms (e.g., ^{87}Rb). Alkali-metal atoms are pumped with a circularly polarized laser light and the transverse angular momentum of them along x is measured using a linearly polarized probe light. The noble-gas nuclear spins are polarized through spin-exchange collisions with optically polarized alkali-metal atoms. A bias magnetic field $B_z^0\hat{z}$ is applied to tune Larmor frequency ν_0 of the nuclear spins.

(3) Saturated case. When B_a is much larger, the term $(\gamma_{\rm n}B_a/2)^2T_{1\rm n}T_{2\rm n}$ is so remarkable that the effective field $\boldsymbol{B}_{\rm eff}^{\rm n}$ can be negligible. In this situation, the linear response of the alkali-metal atoms to the applied oscillating field is dominant.

Apart from the oscillating field amplitude, the effective magnetic field $\boldsymbol{B}_{\rm eff}^{\rm n}$ also depends on the oscillating field frequency ν.

(1) On-resonance case. When $\nu \approx \nu_0$, the effective field $\boldsymbol{B}_{\rm eff}^{\rm n}$ reaches a maximum and could be much larger than the oscillating field amplitude B_a, as shown in Figure 4(a).

(2) Near-resonance case. The effective field increases when the frequency of the oscillating field frequency ν becomes close to the Larmor frequency ν_0. Thus, there is a frequency bandwidth for the spin-based amplifier.

(3) Far-off-resonance case. When $\delta\nu \gg 0$, the term $(2\pi\delta\nu)^2T_{2\rm n}^2$ is dominant in (6). In this situation, the effective field $\boldsymbol{B}_{\rm eff}^{\rm n}$ generated by noble-gas nuclear spins is negligible and the applied oscillating field $B_a\cos(2\pi\nu t)\hat{y}$ is dominant, as shown in Figure 4(b).

2.2 Spin dynamics with a periodically driven AC field along z axis

When an additional magnetic field $B_{\rm ac}\cos(2\pi\nu_{\rm ac}t)\hat{z}$ along z periodically driving the noble-gas spin system, the total magnetic field experienced by noble-gas nuclear spins $\boldsymbol{B} = B_a\cos(2\pi\nu t)\hat{y} + [B_z^0 + B_{\rm ac}\cos(2\pi\nu_{\rm ac}t)]\hat{z}$. This realizes a Floquet system with time-dependent Hamitonians $\mathcal{H}(t+T) = \mathcal{H}(t)$ [28, 29]. The periodically driving makes the time-independent system be a dressed spin system [17], which is characterized by a series of time-independent Floquet states and energy levels that are analogous to the Brillouin-zone artificial dimension [30]. Similarly, by solving the evolution of noble-gas nuclear spins from (5) with the weak field approximation $\gamma_n B_a/2 \ll 1/T_{1\rm n}$, we obtain the steady-state effective field experienced by alkali-metal atoms as [16, 18, 19, 24]

$$\boldsymbol{B}_{\rm f,eff}^{\rm n} = \beta M_0^{\rm n} B_a \left\{ \sum_{l=-\infty}^{+\infty} \sum_{k=-\infty}^{+\infty} B_{k,l}(u,\nu)\cos[2\pi(\nu + l\nu_{\rm ac})t] + A_{k,l}(u,\nu)\sin[2\pi(\nu + l\nu_{\rm ac})t] \right\}, \tag{10}$$

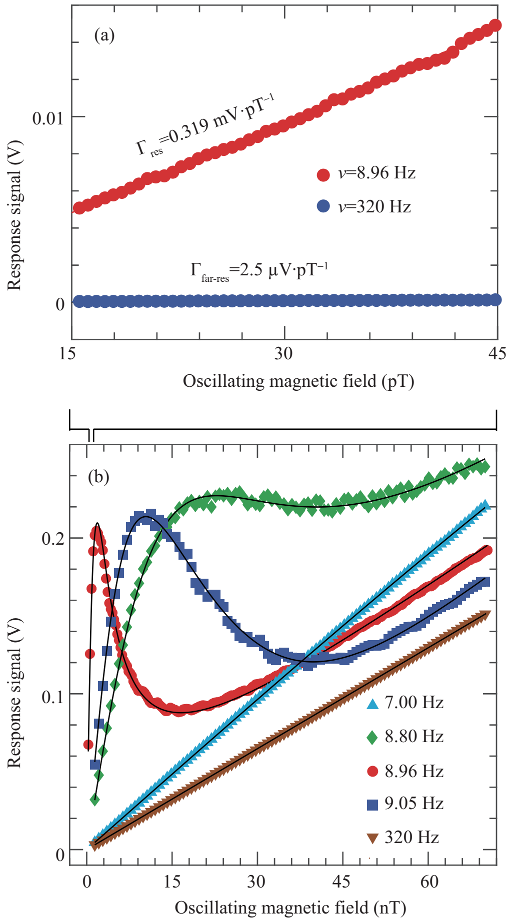

Figure 3 (Color online) Responses of the effective field $\boldsymbol{B}^{\rm n}_{\rm eff}$ as a function of the oscillating field amplitude in the ^{129}Xe-^{87}Rb spin system. (a) The linear signals (red circles, on-resonance; blue circles, far off-resonance) as a function of the oscillating field amplitude. The on-resonance slope $\Gamma_{\rm res} \approx 0.319\pm 0.002$ mV·pT^{-1} is at least two orders of magnitude greater than the far-off-resonance slope $\Gamma_{\text{far-res}} \approx 2.5 \pm 0.1$ μV·pT^{-1}. (b) The nonlinear responses as a function of the oscillating field amplitude. In the near-zero-amplitude regime, the response of the spin-based amplifier is linear, corresponding to the case shown in (a). In the experiments, the bias field is set at $B^0_z \approx 759$ nT, corresponding to the ^{129}Xe Larmor frequency $\nu_0 \approx 8.96$ Hz. The black lines are theoretical fits. Adapted and reprinted with permission from [16].

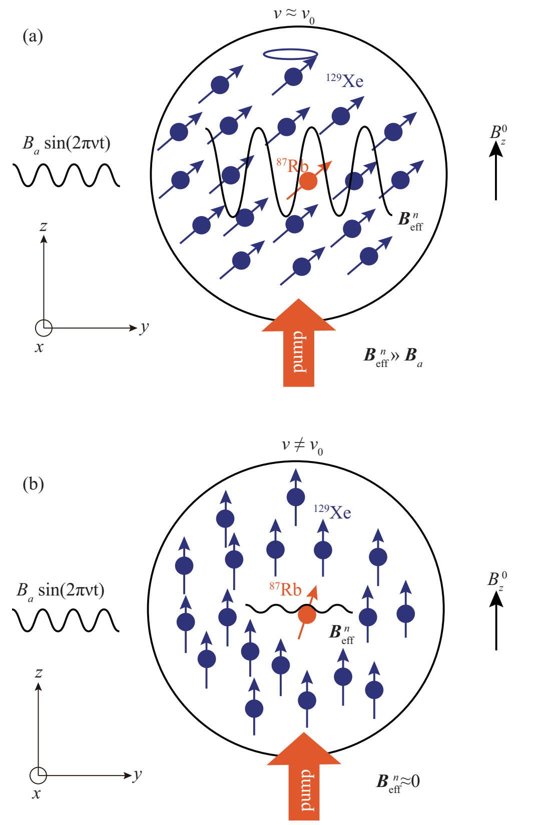

Figure 4 (Color online) Relationship between the effective magnetic field $\boldsymbol{B}^{\rm n}_{\rm eff}$ and the oscillating field frequency ν. (a) When the oscillation frequency ν of an external magnetic field matches the ^{129}Xe Larmor frequency, the ^{129}Xe spin magnetization is tilted away from the z axis and generates a transverse effective field $\boldsymbol{B}^{\rm n}_{\rm eff}$ on ^{87}Rb atoms. Due to the Fermi-contact interaction, the amplification factor defined as $\eta = |\boldsymbol{B}^{\rm n}_{\rm eff}/\boldsymbol{B}_a \gg 1|$ enables significant amplification of the signal from the external magnetic field. (b) In far-off-resonant case, ^{129}Xe spin magnetization is nearly unchanged along z and thus $\boldsymbol{B}^{\rm n}_{\rm eff} \approx 0$. Adapted and reprinted with permission from [16].

where the coefficients $A_{k,l}(u,\nu)$ and $B_{k,l}(u,\nu)$ are

$$\begin{aligned} A_{k,l}(u,\nu) &= \frac{\gamma_n P^{\rm n}_0 T_{2\rm n} J_{k+l}(u) J_k(u)}{2} \frac{1}{1+[2\pi\,(k v_{\rm ac} - \delta\nu)\,T_{2\rm n}]^2}, \\ B_{k,l}(u,\nu) &= \frac{\gamma_n P^{\rm n}_0 T_{2\rm n} J_{k+l}(u) J_k(u)}{2} \frac{2\pi\,(k v_{\rm ac} - \delta\nu)\,T_{2\rm n}}{1+[2\pi\,(k v_{\rm ac} - \delta\nu)\,T_{2\rm n}]^2}, \end{aligned} \tag{11}$$

the modulation index $u = (\gamma_n B_{\rm ac})/\nu_{\rm ac}$ and J_k is the Bessel function of the first kind. In the Floquet spin system, only $P^{\rm n}_y(t)$ is considered because ^{87}Rb magnetometer is primarily sensitive to the magnetic field along y. The physical meaning of these equations is that the transition amplitudes are proportional to the products of the amplitudes of the initial and final Floquet states and a resonant Lorentz factor.

Figure 5(a) shows that under a periodically driving, the intrinsic two-level nuclear spin system (e.g., ^{129}Xe) is extended to an infinite number of synthetic and time-independent energy levels. $|\pm, n\rangle = |\pm\rangle \otimes |n\rangle$ is introduced as the basis states, where n signifies the radio frequency photon number of the

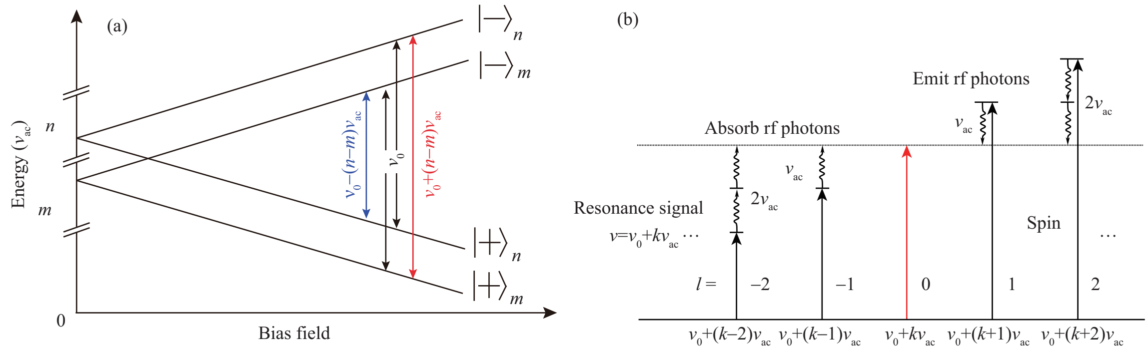

Figure 5 (Color online) (a) Energy levels of a periodically driven two-level system (the Floquet system). (b) The corresponding Floquet states and multiple radio frequency (rf) photon transitions. Adapted and reprinted with permission from [17] Copyright 2021 American Association for the Advancement of Science.

driving field, and $|\pm\rangle$ denotes the eigenstates of the two-level spin system σ_z. The Floquet transition between $|\uparrow\rangle_n$ and $|\downarrow\rangle_m$ states corresponds to an oscillating field with the frequency of $\nu_0 + k\nu_{\rm ac}$ (here $k = n - m$), which forms a sideband around the ^{129}Xe Larmor frequency. Based on (10) and the Lorentz factor in (11), the response of the Floquet system reaches the local maximum in resonant case $k\nu_{\rm ac} = \delta\nu$, which indicates multiple resonance can be realized, as shown in Figure 5(b). Moreover, due to the feasibility to engineer the inherent discrete states and transitions of quantum systems, Floquet systems could be a promising platform to explore advanced quantum amplification beyond ordinary systems with improved performance, for example, in operation bandwidth and frequency tunability.

3 Noble-gas amplification effect

Measuring weak electromagnetic and hypothetical fields assisted by quantum amplification are important for fundamental physics and practical applications including low-noise masers [31,32], ultra-sensitive magnetic resonance spectroscopy [33], weak field and force measurements [34]. In the noble-gas system, the resonant oscillating field can induce an oscillating noble-gas nuclear magnetization, which can generate a considerable effective magnetic field $\boldsymbol{B}^{\rm n}_{\rm eff}$ or $\boldsymbol{B}^{\rm n}_{\rm f,eff}$ on alkali-metal atomic spins, which could be much larger than the applied oscillating field B_a. Due to the weak coupling during collisions (Fermi-contact interactions) between alkali-metal electron spins and noble-gas nuclear spins [2], the nuclear spins can function as an amplifier for the resonant magnetic field and the electron spins act as an atomic magnetometer to measure the enhanced field. To quantify the amplification effect, we define an amplification factor:

$$\eta = |\boldsymbol{B}^{\rm n}_{\rm eff}/\boldsymbol{B}_a|, \quad \eta_f = |\boldsymbol{B}^{\rm n}_{\rm f,eff}/\boldsymbol{B}_a| \tag{12}$$

for the inherent and Floquet systems, respectively.

3.1 Spin amplification

We first derive the amplification factor η on resonance for the inherent system. When $(\gamma_{\rm n}B_a/2)^2T_{1\rm n}T_{2\rm n} \ll 1$, the spin-based amplifier works in the sensitive linear-response regime and $\boldsymbol{B}^{\rm n}_{\rm eff}$ in (6) can be written as

$$\boldsymbol{B}^{\rm n}_{\rm eff}(\nu = \nu_0) = \frac{1}{2}\beta M^{\rm n}_0 P^{\rm n}_0 \gamma_{\rm n} T_{2\rm n}[\cos(2\pi\nu t)\hat{x} + \sin(2\pi\nu t)\hat{y}]B_a. \tag{13}$$

Thus the effective field $\boldsymbol{B}^{\rm n}_{\rm eff}$ is a circularly polarized field and its amplitude is equal to $\frac{1}{2}\beta M^{\rm n}_0 P^{\rm n}_0 \gamma_{\rm n} T_{2\rm n} \cdot B_a$. As a result, the amplification factor is

$$\eta = \frac{1}{2}\beta M^{\rm n}_0 P^{\rm n}_0 \gamma_{\rm n} T_{2\rm n}. \tag{14}$$

From (14), there are various methods to increase the amplification factor, such as prolonging relaxation time $T_{2\rm n}$ and improving equilibrium polarization $P^{\rm n}_0$. Based on the calculation in [16, 18, 19], the amplification factor can be as large as 10^4 in a ^{3}He-K system. The sensitivity of ^{3}He-K magnetometer can be improved by four orders of magnitude and potentially reach a few aT/Hz$^{1/2}$.

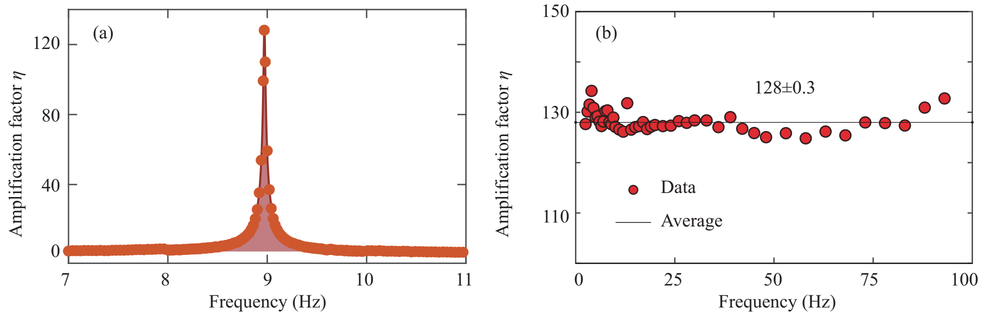

Figure 6 (Color online) Calibration of the spin amplification factor in the ^{129}Xe-^{87}Rb spin system. (a) The frequency-response of the ^{87}Rb magnetometer to oscillating fields along y, assisted with ^{129}Xe spin-based amplifier. The experimental data (red circles) are obtained by scanning the auxiliary field frequencies. The solid line is the theoretical fit of the data and agrees well with the experiment. (b) The measured amplification factor η at different resonance frequencies. The average η is measured to be $\eta \approx 128 \pm 0.3$. Adapted and reprinted with permission from [16].

The amplification factor η is experimentally calibrated by the following steps.

(i) A resonant oscillating field is applied along y. The output signal of the alkali-metal magnetometer is recorded and its amplitude

$$A(\boldsymbol{B}_{\mathrm{eff}}^{\mathrm{n}}) \propto P_x^{\mathrm{e}}(\boldsymbol{B}_{\mathrm{eff}}^{\mathrm{n}}) \propto \eta \frac{1}{\sqrt{[(B_z^0)^2 + (\Delta B)^2]}} B_a. \tag{15}$$

Because the exact Larmor frequency is generally unknown without prior calibration, an alternative way is to scan the oscillating field frequency over a small frequency range, corresponding to the narrow bandwidth $\sqrt{3}\Lambda$ of the spin-based amplifier from the on-resonant effective field

$$|\boldsymbol{B}_{\mathrm{eff}}^{\mathrm{n}}| \propto \frac{\Lambda/2}{\sqrt{(\delta\nu)^2 + (\Lambda/2)^2}}. \tag{16}$$

(ii) A far-off-resonant oscillating field is applied along y. Similarly, we record the amplitude $A(B_a\hat{y})$ of the output signal of the alkali-metal magnetometer:

$$A(B_a\hat{y}) \propto P_x^{\mathrm{e}}(B_a\hat{y}) \propto \frac{\Delta B}{[(B_z^0)^2 + (\Delta B)^2]} B_a. \tag{17}$$

Note that the frequency of the far-off-resonant field should be within the bandwidth of the magnetometer.

(iii) By calculating the ratio of the above two amplitudes $\Phi(\nu_0) = A(\boldsymbol{B}_{\mathrm{eff}}^{\mathrm{n}})/A(B_a\hat{y})$, we have

$$\eta = \Phi(\nu_0) \Big/ \sqrt{1 + \left(\frac{\nu_0}{\gamma_n \Delta B}\right)^2}. \tag{18}$$

Figure 6(a) shows the experimental results for the frequency-response of the ^{87}Rb magnetometer and the calibration of the spin amplification factor in the ^{87}Rb-^{129}Xe system. In the experiments, the bias field B_z^0 is set as ≈ 759 nT and the Larmor frequency $\nu_0 \approx 8.96$ Hz is experimentally calibrated using the ^{129}Xe free-decay signal due to the residual magnetic field and effective field of ^{87}Rb atoms. An oscillating magnetic field of 30 pT is applied along y. As shown in Figure 6(a), the signal amplitude is well described by a single-pole band-pass filter model [16], yielding the full width at half maximum (FWHM) of 52 mHz. The amplification factors at different resonance frequencies are calibrated and their average is 128 ± 0.3, as shown in Figure 6(b).

It is worthy to point out, that although the spin amplification with nuclear spins is demonstrated in previous studies [22, 35], the current detection schemes are totally different. Previous studies all consider the "remote" readout scheme, where the nuclear magnetization is measured from a distance with atomic or SQUID magnetometers. In contrast, the spin amplification demonstrated here uses a "contact" readout scheme where the polarized nuclei and the detector are spatially overlapping in the same vapor cell. The magnetic field at position $\boldsymbol{r}$ generated by nuclear magnetization in these two cases is

$$\boldsymbol{B}(\boldsymbol{r}) = \overbrace{\frac{\mu_0}{4\pi} \frac{3\hat{r}(\hat{r} \cdot \boldsymbol{m}) - \boldsymbol{m}}{r^3}}^{\text{“remote”}} + \overbrace{\frac{2\mu_0 \boldsymbol{m}}{3}}^{\text{“contact”}} \delta(\boldsymbol{r}), \tag{19}$$

where $\boldsymbol{m}$ is the magnetic dipole moment. The "contact" term in (19) corresponds to the noble-gas effective magnetic field $\boldsymbol{B}_{\rm eff}^{\rm n}$ described by the Fermi-contact interactions. This "contact" readout scheme offers a significant advantage: a considerable effective magnetic field is induced from the magnetization of noble-gas nuclear spins due to the large Fermi-contact enhancement factor and measured *in situ* with an atomic magnetometer. In contrast, it is experimentally challenging to prepare high nuclear-spin polarization and maintain readout sensitivity for the "remote" scheme.

3.2 Floquet spin amplification

Based on (10)–(12), we can obtain the Floquet amplification factors η_f for the Floquet system:

$$\eta_f(u,\nu)=\beta M_0^{\rm n}\sqrt{\left(\sum_{k=-\infty}^{+\infty}A_{k,l}(u,\nu)\right)^2+\left(\sum_{k=-\infty}^{+\infty}B_{k,l}(u,\nu)\right)^2}. \tag{20}$$

When the oscillation frequency of the measured field matches with one of Floquet transitions $\delta\nu+kv_{\rm ac}\approx 0$, the amplification effect becomes significant. The Floquet amplification factors are

$$\eta_{k,l}(u)=\frac{1}{2}\beta M_0^{\rm n}P_0^{\rm n}\gamma_n T_{2\rm n}J_{k+l}(u)J_k(u), \tag{21}$$

where k and l are used to describe the frequencies of the measured and amplified fields. Specifically, k denotes that the measured field frequency is at $\nu=\nu_0+k\nu_{\rm ac}$, and l denotes that the output signal frequency is at $\nu_0+(k+l)\nu_{\rm ac}$. For $k=1$, the spectral amplitude of each sideband (transitions between Floquet states) is shown in Figure 7(a). Although the test frequency matches only one Floquet transition (marked with a star), there simultaneously exist amplification signals at other Floquet transitions. These sidebands are similar to frequency comb composed of equidistant narrow lines, and can be seen as the result of the field photons scattered by driven ^{129}Xe spins through the virtual absorption and emission of radio frequency (rf) photons. The experimental measured ratio among different transitions is $\eta_{1,-1}:\eta_{1,0}:\eta_{1,1}:\eta_{1,2}\approx 1:0.916:1.480:0.987$, which is close to the theoretical value $|J_0(u)|:|J_1(u)|:|J_2(u)|:|J_3(u)|=1:0.984:1.631:1.107$.

There is a particular but common example, when $l=0$, the measured field and amplified signal are both at $\nu=\nu_0+k\nu_{\rm ac}$. In this case, the amplification factor is given by

$$\eta_{k,0}(u)=\frac{1}{2}\beta M_0^{\rm n}P_0^{\rm n}\gamma_n T_{2\rm n}J_k^2(u). \tag{22}$$

For the case of $l\neq 0$, the applied and detected frequencies are different. The experimental result is shown in Figure 7(b) and the ratio among different transitions is close to the theoretical value $J_0^2(u):J_{\pm 1}^2(u):J_{\pm 2}^2(u):J_{\pm 3}^2(u)=1:0.969:2.660:1.225$.

Based on (21) and (22), the measured frequency ν should satisfy $\nu\approx\nu_0+k\nu_{\rm ac}$, where k is an integer, otherwise, the amplification factor is small. Therefore, the profile of the amplification can be written as

$$\eta(u,\nu)=\sum_k J_k^2(u)\frac{\frac{1}{2}\beta M_0^{\rm n}P_0^{\rm n}\gamma_n T_{2\rm n}}{\sqrt{1+\left[2\pi\left(\delta\nu+kv_{\rm ac}\right)T_{2\rm n}\right]^2}}, \tag{23}$$

which is a sum of resonance with the full-width at half-maximum (FWHM) for each amplification regime being $\sqrt{3}/(\pi T_{2\rm n})$. In experiments, the FWHM is generally on the order of MHz. Note that the amplification profile depends on the modulation index u. In this case, the Bessel function of the first kind satisfies $J_0(0)=1$ and $J_k(0)=0$ for $k>0$. Then, Eq. (23) can be reduced to (14), which is in good agreement with the theory. The Floquet spin amplification allows the detection of the signal at multiple different regimes. In contrast, the spin amplification is aimed to detect a single oscillating field. Table 1 summarizes the main difference between the cases with/without periodic driving.

4 Noble-gas masing effect

Maser (microwave amplification by stimulation emission of radiation) is a device or object that emits coherent electromagnetic radiation (mainly in the microwave region) produced by the natural oscillations

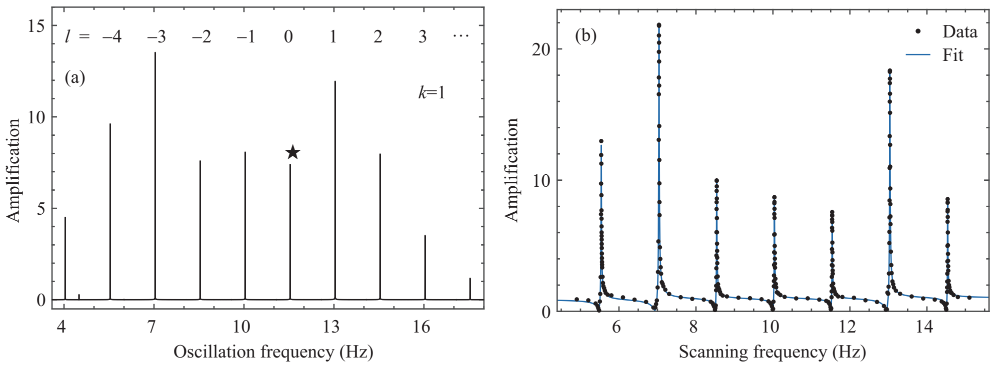

Figure 7 (Color online) Floquet spin amplification. (a) Spectrum of the amplified signal induced by an applied field with the oscillation frequency set at the frequency of 1st-order sideband (see star). Other sideband signals are simultaneously induced. The amplification satisfies $\eta_{k,l}$. (b) Plot of amplification as a function of the scanning oscillation frequency of the applied magnetic field. The interval between the amplified peaks is equal to $\nu_{\rm ac}$. The amplification at each resonance frequency satisfies $\eta_{k,0}$. The amplification profile is asymmetric due to the Fano interference [24]. Here $B_z^0 \approx 853$ nT, $B_{\rm ac} \approx 397$ nT, $\nu_{\rm ac} \approx 1.500$ Hz. Adapted and reprinted with permission from [24].

Table 1 Comparison between the driven case and the undriven case

	With the periodic driving	Without the periodic driving
Modulation index u	> 0	0
Resonance frequency	$\nu \approx \nu_0 + k\nu_{\rm ac}$	$\nu \approx \nu_0$
l-AC-photon transition amplitude	$\propto J_{k+l}(u)J_k(u)$	No AC-photon transition
Amplification factor	$\eta_{k,l}(u) = \frac{1}{2}\beta M_0^{\rm n} P_0^{\rm n} \gamma_{\rm n} T_{2\rm n} J_{k+l}(u) J_k(u)$	$\eta = \frac{1}{2}\beta M_0^{\rm n} P_0^{\rm n} \gamma_{\rm n} T_{2\rm n}$

of atoms or molecules between energy levels [32, 36, 37]. The maser operates based on the same basic principle as the laser (light amplification by stimulated emission of radiation), which generates higher frequency coherent radiation at visible wavelengths and shares many of its characteristics. The first maser was built by the American physicist Townes [38] and his colleagues in 1953. Because the frequency of radio waves produced by masers is highly stable, masers can be used as the timekeeping device or high precision frequency references in atomic clocks [39], and as extremely low-noise microwave amplifiers in radio telescopes and deep space spacecraft communication ground stations [33].

In Section 3, we have demonstrated the basic principle of the spin-based amplifiers that produces an amplification of the applied oscillating magnetic fields in magnitude, when oscillation frequency matches its natural or Floquet energy levels of the nuclear spins. Moreover, based on the spin amplification, noble-gas nuclear spins can be used as the masing medium and feedback is created to produce coherent radiation. Figure 8 shows the experimental setup for realizing the noble-gas masing effect, most of which is the same as the spin-based amplifiers, except for a feedback circuit [17]. Similar to a microwave cavity in conventional masers, the nuclear spins (e.g., ^{129}Xe) are embedded in a feedback circuit, while the atomic magnetometer is a sensitive detector of nuclear spins to measure the nuclear spin polarization $P_x^{\rm n}$ along the x direction.

The real-time output signal of the magnetometer generates the feedback field $B_{\rm f}(t) = \chi P_x^{\rm n}(t)$ on noble-gas nuclear spins along y, which is applied to the nuclear spins with a set of y coils around the vapor cell. Here the proportionality constant χ (feedback gain) encapsulates the conversion factor of the atomic magnetometer, the Fermi-contact interactions and the connection polarity of the feedback coils. The amplitude of feedback gain χ can be adjusted with a rheostat in series with the feedback coils. The sign of feedback gain χ is simultaneously determined by the direction of the bias magnetic field ($+z$, or $-z$) and the connection polarity of the feedback coils ($+y$, or $-y$), i.e., ($+z$, $-y$), ($-z$, $+y$) for $\chi > 0$ and ($-z$, $-y$), ($+z$, $+y$) for $\chi < 0$. Similar to a resonant cavity [40], the self-induced feedback field $B_{\rm f}(t)$ carries the information about the spins and then acts back on the spins, leading to the well-known phenomenon of damping [33, 41] that is important in our maser scheme.

With the feedback circuit, the dynamics of the ^{129}Xe spin polarization $\boldsymbol{P}^{\rm n} = [P_x^{\rm n}, P_y^{\rm n}, P_z^{\rm n}]$ is described

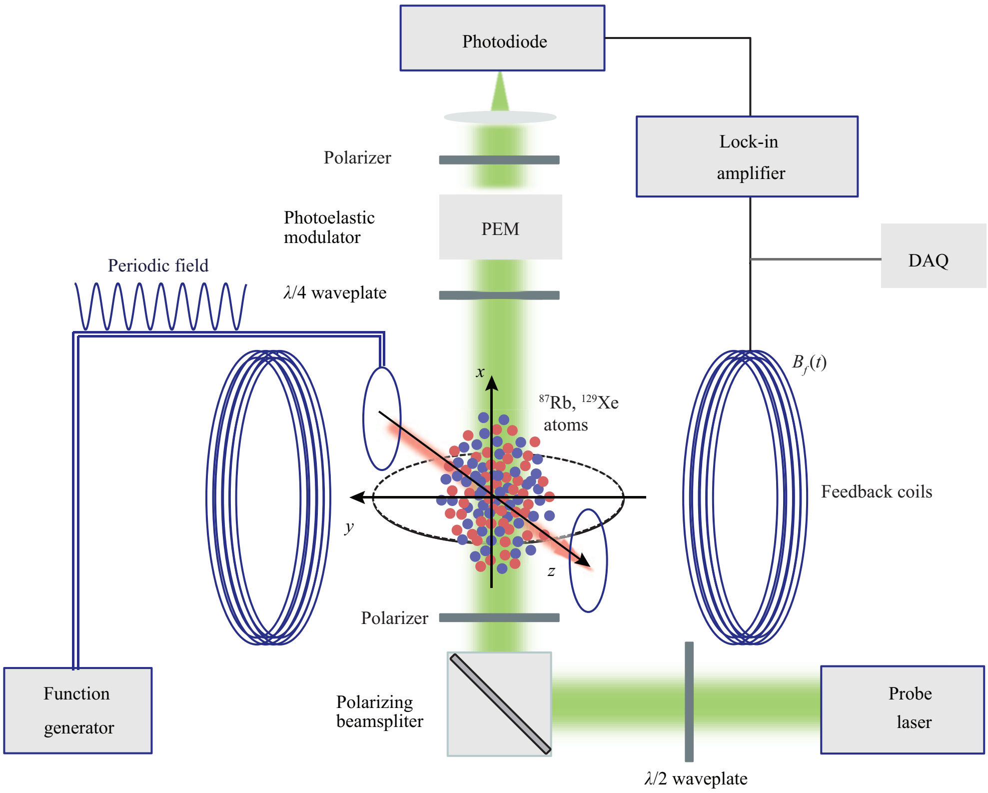

Figure 8 (Color online) Schematic of the experimental setup for the masing effect in the noble-gas spin system (e.g., the ^{129}Xe-^{87}Rb system). The noble-gas nuclear spins are polarized and detected by spin-exchange collisions with optically pumped alkali-metal atoms. Under a bias field and an oscillating magnetic field along z, the nuclear spins are magnetically coupled to a feedback circuit, which feeds back real-time $B_{\rm f}(t)$ along y and induces the damping of nuclear spins. Adapted and reprinted with permission from [17] Copyright 2021 American Association for the Advancement of Science.

by the nonlinear Bloch equations [33, 42]:

$$\begin{cases} \frac{{\rm d}P_x^{\rm n}}{{\rm d}t} = P_y^{\rm n}2\pi\nu_z(t) - P_z^{\rm n}2\pi\nu_y(t) - \frac{1}{T_{\rm 2n}}P_x^{\rm n}, \\ \frac{{\rm d}P_y^{\rm n}}{{\rm d}t} = P_z^{\rm n}2\pi\nu_x(t) - P_x^{\rm n}2\pi\nu_z(t) - \frac{1}{T_{\rm 2n}}P_y^{\rm n}, \\ \frac{{\rm d}P_z^{\rm n}}{{\rm d}t} = P_x^{\rm n}2\pi\nu_y(t) - P_y^{\rm n}2\pi\nu_x(t) - \frac{1}{T_{\rm 1n}}P_z^{\rm n} + \gamma_{\rm se}(P_z^{\rm e} - P_z^{\rm n}), \end{cases} \tag{24}$$

where $2\pi[\nu_x(t), \nu_y(t), \nu_z(t)] = \gamma_n/[B_z^0 + B_{\rm ac}\cos(2\pi\nu_{\rm ac}t)]\hat{z} + \gamma_n B_{\rm f}(t)\hat{y}$. As the thermal nuclear spin polarization is much smaller than that from spin-exchange collisions, we can neglect the thermal polarization in (24). The gain is $\chi = 0$ when the feedback circuit is disabled. $P_z^{\rm e}$ is the polarization of the rubidium atoms, which depends on the optical pumping and spin-relaxation rates [2]. $\gamma_{\rm se}$ is the spin-exchange rate between the nuclear spins and the alkali-metal atoms. $\gamma_{\rm se}(P_z^{\rm e} - P_z^{\rm n})$ represents the spin-exchange pumping of nuclear spins. The spin dynamics is obtained by solving (24).

4.1 Spin maser

We consider the case without the periodically driving, i.e., $B_{\rm ac} = 0$. As damping is important to realize masers [33, 41, 42], the feedback-induced damping of nuclear spins is first investigated. There are two cases of the spin dynamics.

(1) When $P_z^{\rm n} > 0$, $\chi < 0$ or $P_z^{\rm n} < 0$, $\chi > 0$, stationary maser dynamics cannot be generated. The noble-gas nuclear spins are initially polarized to an equilibrium state along z by spin-exchange pumping, and then titled by a small angle θ_0 with a magnetic field pulse along x. From (24), the evolution of the spin polarization $\boldsymbol{P}^{\rm n}$ becomes [33, 42]

$$\begin{aligned} P_+^{\rm n}(t) &= P_0^{\rm n}T_{\rm d}\frac{Q}{T_{\rm 2n}}{\rm sech}\left[\frac{q}{T_{\rm 2n}}(t-t_0)\right]{\rm e}^{{\rm i}(2\pi\nu t-\pi/2)}, \\ P_z^{\rm n}(t) &= P_0^{\rm n}T_{\rm d}/T_{\rm 2n}\left\{q{\rm tanh}\left[\frac{q}{T_{\rm 2n}}(t-t_0)\right]-1\right\}, \end{aligned} \tag{25}$$

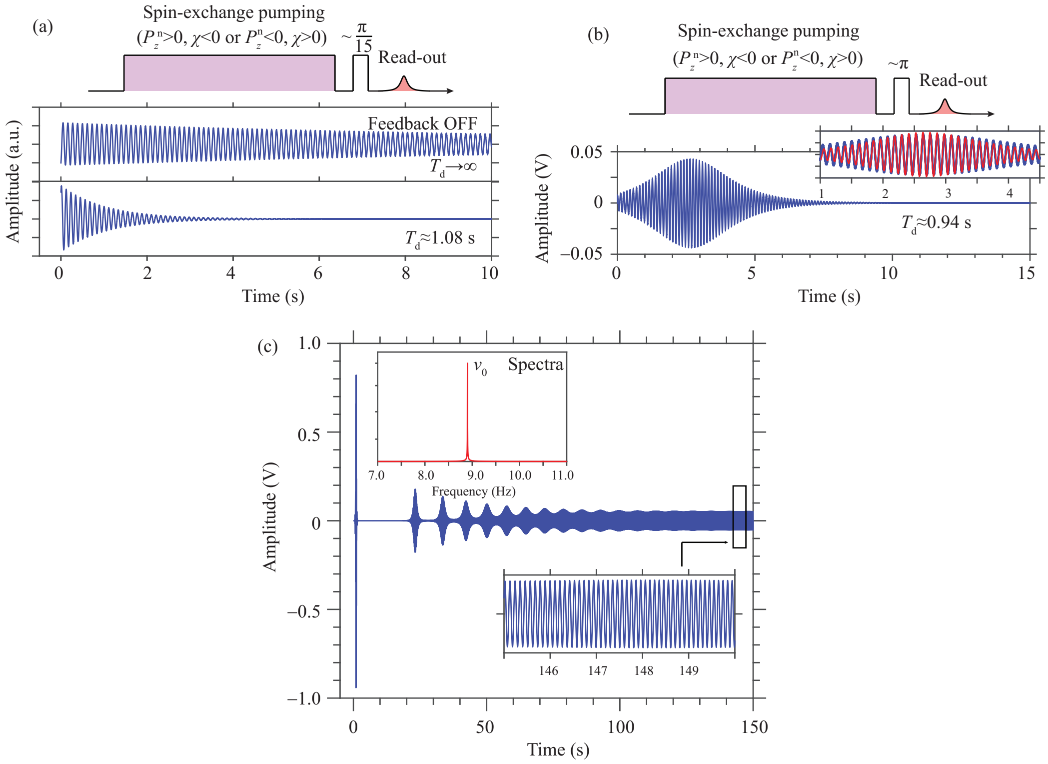

Figure 9 (Color online) Experimental test for damping feedback mechanism in ^{129}Xe-^{87}Rb system. (a) Measured free decay ^{129}Xe signals for different feedback gains (corresponding to different T_d). Here the spin population P_z and the feedback gain χ are initially set as $P_z > 0$, $\chi < 0$ or $P_z < 0$, $\chi > 0$. T_d is well determined by corresponding decay time T_2 with $\sim \frac{\pi}{15}$ excitation angle. (b) Transient maser operations after flipping $\sim \pi$ angle, inducing the inversion of ^{129}Xe spins population. The decay signal can be fitted with a hyperbolic secant function shown in the inset. (c) Time-domain signal and spectrum of ^{129}Xe maser (i.e., $\nu_\mathrm{ac} = 0$). The lower inset is zoom-in plots for the signal. The upper inset is the corresponding amplitude spectra of the maser signal after eliminating the transient. Adapted and reprinted from [17] Copyright 2021 American Association for the Advancement of Science.

where $P_+^\mathrm{n} = P_x^\mathrm{n} + \mathrm{i}P_y^\mathrm{n}$, ν is the oscillation frequency, and

$$\begin{aligned} q &= [1 + (T_{2\mathrm{n}}/T_\mathrm{d})^2 + 2\cos\theta_0(T_{2\mathrm{n}}/T_\mathrm{d})]^{1/2}, \\ t_0 &= -\frac{T_{2\mathrm{n}}}{q}\tanh^{-1}\left[\frac{1}{q}\left(\frac{T_{2\mathrm{n}}}{T_\mathrm{d}}\cos\theta_0 + 1\right)\right]. \end{aligned} \tag{26}$$

Here the intrinsic decoherence time $T_{2\mathrm{n}}$ and the damping time T_d depend on feedback gain χ. In this case, the free decay signal can be fitted with a single-exponential decay with a decay rate given by $T_{2\mathrm{n}}^{-1} + T_\mathrm{d}^{-1}$. This shows that, by coupling nuclear spins to the feedback circuit, a regime can be reached in which damping constitutes the dominant mechanism of spin relaxation, e.g., $T_\mathrm{d} \ll T_{2\mathrm{n}}$, and spin relaxation can be controlled by adjusting the feedback gain, as shown in Figure 9(a). Note that longitudinal relaxation is neglected here. $|P_+^\mathrm{n}(t)|$ reaches its maximum value at $t = t_0$. Moreover, the oscillation frequency has a small shift from the Larmor frequency ν_0, i.e., $\nu = \nu_0 + \Delta\nu$ with $\Delta\nu = \alpha \cdot 1/T_\mathrm{d}$, arising from an effect known as frequency pulling [42].

When the nuclear spin population is suddenly inverted, i.e., $\theta_0 \approx \pi$, unlike the exponential decay, for $T_\mathrm{d}/T_{2\mathrm{n}} \geqslant 1$, then $t_0 \leqslant 0$, and thus $|P_+^\mathrm{n}(t)|$ should be monotonically decreasing; for $T_\mathrm{d}/T_{2\mathrm{n}} < 1$, then $t_0 > 0$, and $|P_+^\mathrm{n}(t)|$ increases to be maximum at $t = t_0$ and then decreases to be zero, which can be described by a hyperbolic secant function, as shown in Figure 9(b). As first reported in [41], this is a transient maser when the threshold of the damping time $T_\mathrm{d}/T_{2\mathrm{n}} \ll 1$ is fulfilled. However, the transient maser cannot oscillate continuously because the population inversion is transient. In order to generate stationary maser dynamics [31, 37, 43], we can reverse the circular polarization of pump laser, or alternatively reverse the sign of the feedback gain χ, and simultaneously set the damping time smaller than the intrinsic decoherence time (i.e., $T_\mathrm{d}/T_{2\mathrm{n}} < 1$).

(2) When $P_z^\mathrm{n} > 0$, $\chi > 0$ or $P_z^\mathrm{n} < 0$, $\chi < 0$ and $T_\mathrm{d}/T_{2\mathrm{n}} < 1$, stationary maser dynamics is generated. Under these conditions, coupling of the spins to the damping feedback circuit can produce a self-sustained

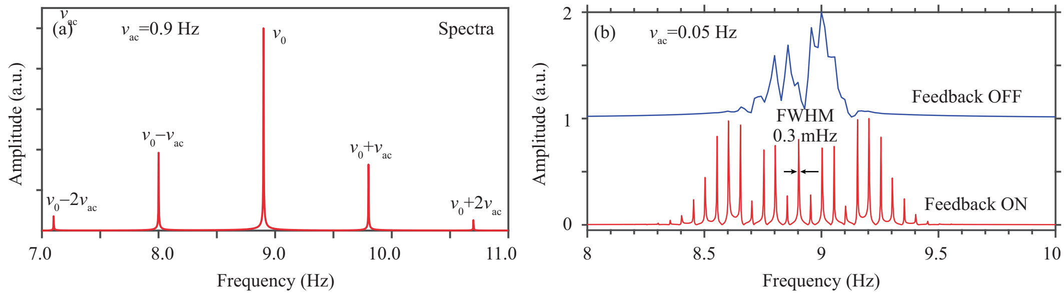

Figure 10 (Color online) (a) Amplitude spectrum of ^{129}Xe Floquet maser for $\nu_{\rm ac} = 0.9$ Hz. (b) Comb-like ultrahigh-resolution spectroscopy of Floquet maser for $\nu_{\rm ac} = 0.05$ Hz. The sideband spectrum (red line) exhibits at least 25 evident comb-like symmetric lines centered at the Larmor-frequency line at ν_0. Floquet transitions can build up stationary maser oscillations in the strong-coupling regime ($\gamma B_{\rm ac}/\nu_{\rm ac} \gg 1$), enabling exact reconstruction of the Floquet energy levels. Here $B_{\rm ac} = 56.15$ nT. Adapted and reprinted with permission from [17] Copyright 2021 American Association for the Advancement of Science.

masing signal [33, 42]. The stationary solution of (24) can be obtained as

$$\begin{aligned} P_x^{\rm n} &= \sqrt{(1/T_{\rm 1n} + \gamma_{\rm se})\left(\frac{1}{T_d} - \frac{1}{T_{\rm 2n}}\right)} T_d P_0^{\rm n} \cos 2\pi\nu_0 t, \\ P_y^{\rm n} &= \sqrt{(1/T_{\rm 1n} + \gamma_{\rm se})\left(\frac{1}{T_d} - \frac{1}{T_{\rm 2n}}\right)} T_d P_0^{\rm n} \sin 2\pi\nu_0 t. \end{aligned} \tag{27}$$

Eq. (27) represents that the noble-gas nuclear spins process at the frequency ν_0 with a non-attenuating amplitude and form a steady maser. Figure 9(c) shows the time-domain masing signal and spectrum of the ^{129}Xe maser measured in ^{129}Xe-^{87}Rb system. Based on numerical simulations, we find that small transverse polarization component caused by misalignment or quantum fluctuation is sufficient for activating the maser.

4.2 Floquet spin maser

We now consider the spin dynamics of the Floquet spin system, i.e., $B_{\rm ac} \neq 0$, under the damping feedback field. The Floquet system can be treated as a time-independent one with an infinite set of energy levels, shown in Figure 5(a). The key to a maser based on Floquet systems is the preparation of spin population between those Floquet states. In our experiments, populations between Floquet states ($|+\rangle_n$ and $|-\rangle_m$) of the Floquet nuclear spins can be continuously prepared through the noble-gas spin-exchange collisions. The threshold of $T_{\rm d}/T_{\rm 2n} < 1$ is satisfied by adjusting the feedback gain χ. When the feedback circuit is suddenly on, a feedback $B_{\rm f}(t)$ is induced by the Floquet system itself and oscillates with the frequencies of Floquet sidebands. The feedback field produces a torque on the spins that change spin polarization [33,42]. This self-coupling can lead to stimulated Rabi oscillations between the Floquet states $|+\rangle_n$ and $|-\rangle_m$ and a steady-state maser oscillation is built up. For different Floquet states pair n, m, the maser oscillation frequency is $E_{n,m}/2\pi = (n - m)\nu_{\rm ac} + \nu_0$.

Recently, the first experimental demonstration of a "Floquet maser" is successfully achieved with periodically driven ^{129}Xe spins [17]. The experimental results are shown in Figures 10(a) and (b). In contrast to conventional masers exploiting inherent transitions [28, 33], the Floquet maser oscillates at the frequencies of transitions between Floquet states. Multi-frequency ultrahigh-resolution spectra of the maser are observed with the bandwidth 0.3 mHz, which is two orders of magnitude narrower than the decoherence-limited resolution. Compared to conventional masers, the Floquet maser has several advantages. First, the Floquet maser generates sidebands that are easily tunable by changing the frequency and amplitude of the periodic driving field. Therefore, it is well-suited for sensing oscillating driving field with an ultrahigh frequency resolution beyond the masing spin decoherence limit. Second, unlike the conventional maser that uses a microwave cavity, the Floquet maser makes use of a feedback circuit based on the signal of an atomic magnetometer to provide damping feedback, enabling the masing frequency down to the audio-frequency range. Although the oscillation frequency is much smaller than that of earlier established microwave masers, the concept of the Floquet maser also be generalized into other frequency ranges.

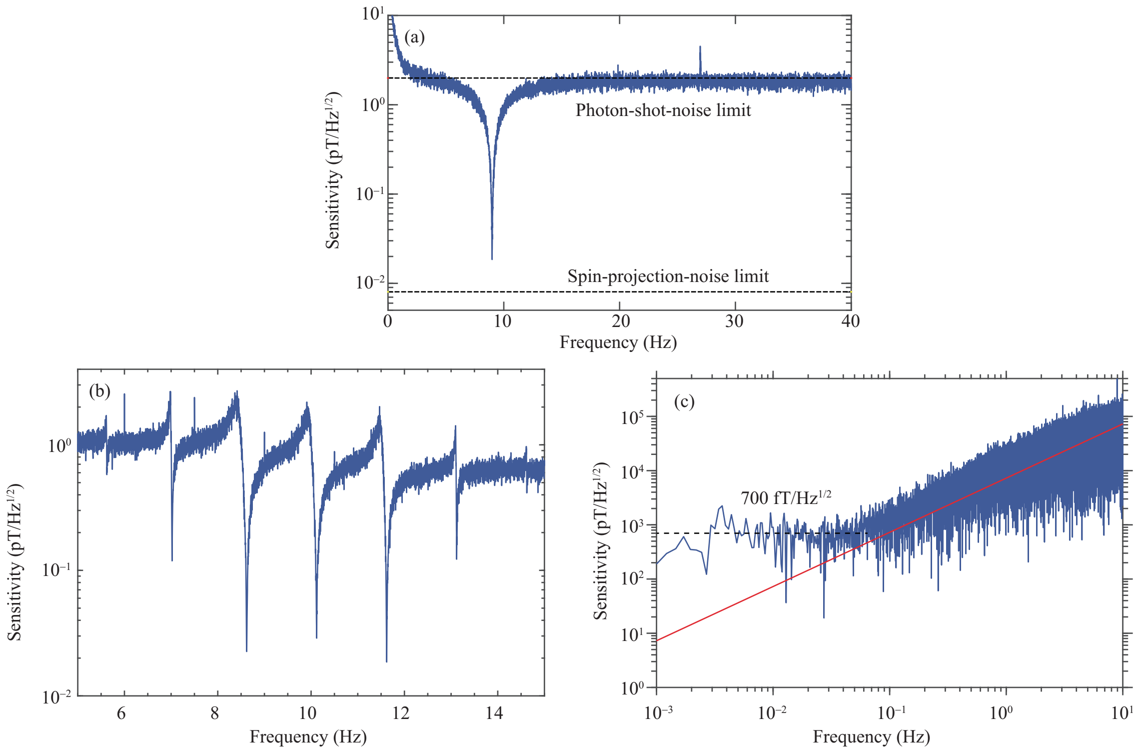

Figure 11 (Color online) Ultrasensitive magnetic-field sensing. (a) Magnetic sensitivity of the spin-amplifier-based magnetometer. 18 fT/Hz$^{1/2}$ is achieved at ^{129}Xe Larmor frequency, which is beyond the photon-shot-noise limit and comparable to the spin-projection-noise limit of the ^{87}Rb magnetometer itself. (b) Magnetic sensitivity of the Floquet-amplification-based magnetometer. The bias field and periodic driving field are set as $B_z^0 \approx 853$ nT, $B_{\rm ac} \approx 178$ nT, $\nu_{\rm ac} \approx 1.500$ Hz. The corresponding modulation index is $u \approx 1.4$. The sensitivity is about 20 fT/Hz$^{1/2}$, 25 fT/Hz$^{1/2}$, 18 fT/Hz$^{1/2}$ at $\nu_0 - 1.5$, ν_0, $\nu_0 + 1.5$, respectively. (c) Magnetic sensitivity of the Floquet-maser-based magnetometer. 700 fT/Hz$^{1/2}$ is achieved and is currently the best sensitivity for the frequency range from 1 to 100 mHz. Adapted and reprinted with permission from [16, 17, 24].

5 Applications

The features of ultrahigh resolution spectra in the maser and ultrahigh sensitivity in the alkali-metal magnetometer with the spin amplification technique could be particularly useful for precision measurements. Unlike previous magnetometers that directly measure external magnetic fields, the amplification-based magnetometer first preamplifiers measured fields through noble-gas spins and then measures the amplified field. In the following, we will review the related applications of the noble-gas spin amplification on magnetic field sensing [44] and searching for ultralight new particles [22, 45, 46]. The experimental demonstration for these applications in this section was carried out on the ^{129}Xe-^{87}Rb system.

5.1 Magnetic-field sensing

Sensitive detection of weak magnetic fields is crucial to various applications, ranging from magnetoencephalography, magnetocardiography, and gyroscopes to space exploration [10, 47–49]. Atomic magnetometers are one of the most sensitive methods, such as nonlinear magneto-optical rotation (NMOR) magnetometer [50] and spin-exchange relaxation-free (SERF) magnetometer [49, 51, 52]. Unlike atomic magnetometers that mostly use electron spins of alkali-mental atoms, nuclear spins of noble gas are another ideal active medium for ultrasensitive magnetic-field sensing because they can maintain coherence for hours under ambient conditions. However, the sensitivity of previous magnetometers demonstrated with nuclear spins is limited to several picotesla levels for their remote read-out schemes where nuclear spins are measured from a distance with atomic and SQUID magnetometers. In this case, it is experimentally challenging to prepare high nuclear-spin polarization and maintain readout sensitivity [35, 46].

With a spin-based amplifier that enhances the measured oscillating field with the amplification factor $\eta \approx 128$, we achieved a magnetic sensitivity of 18 fT/Hz$^{1/2}$ at the resonance frequency in the ^{129}Xe-^{87}Rb system [16], as shown in Figure 11(a), whereas the sensitivity of ^{87}Rb magnetometer is only about 2 pT/Hz$^{1/2}$. The experiment showcases the capability of our sensor to surpass the photon-shot-noise limit of the rubidium magnetometer itself, approaching the spin-projection-noise limit of the latter. Moreover, the sensing technique is significantly better than that of the other state-of-the-art magnetometers demonstrated with nuclear spins, which are limited to a few picotesla sensitivity. Such a spin-based amplifier remains subpicotesla-level sensitivity to the oscillating magnetic fields ranging from 1 Hz to 1 kHz.

Furthermore, the Floquet amplification technique is capable of simultaneously measuring magnetic fields at Floquet transitions. Figure 11(b) shows the case of a 1.5-Hz periodic driving and modulation index $u \approx 1.4$ [24]. The achieved magnetic sensitivity is about 20, 25, 18 $\mathrm{fT/Hz^{1/2}}$ at $\nu_0 - 1.5$, ν_0, $\nu_0 + 1.5$, respectively. Our result illustrates that the magnetic sensitivity can be simultaneously enhanced to $\mathrm{fT/Hz^{1/2}}$ level at frequencies of transitions between Floquet spin states. This yields one order of magnitude improvements over previously achievable detection bandwidth [16,18]. Moreover, the sensitivity at different Floquet-transition frequencies can be controlled through changing the modulation index. Simultaneous measurement at multi-frequency Floquet transitions is similar to that there are multiple detectors working in parallel. Therefore, a properly designed Floquet measurement protocol can greatly speed up the total measurement time [24].

Moreover, experimental investigations have been reported towards achieving high sensitivity of measuring magnetic fields in low-frequency regime (1–100 MHz), which is of importance in applied [44] and fundamental physics [22,45,46]. However, it still remains challenging for state-of-the-art magnetometers to reach femtotesla-level sensitivity owing to significant $1/f$ noise. Using the Floquet maser technique with magnetometry, we modulate the low-frequency signal to the high-frequency sidebands in Floquet masing spectroscopy to suppress the low-frequency noise and realize a sensitive magnetometer with $700\,\mathrm{fT/Hz^{1/2}}$ in the ultra-low frequency range (1–100 MHz), as shown in Figure 11(c). It would be possible to further improve sensitivity by eliminating the technical sources of maser instability, adjusting the amplification factor, and so on. The idea of the Floquet-maser-based magnetometer is that the measured oscillating field applied to the spins can be seen as a periodic driving that generates sidebands around the maser oscillation frequency ($\nu_0 \gg 1$ Hz). Thus, the maser up-converts the low-frequency field to a higher frequency, where the $1/f$ noise arising from ^{87}Rb magnetometer is spectrally separated from the maser signal.

5.2 Searches for new physics

Recently, there is growing interest in developing low-energy precision measurements to discover light and ultralight hypothetical particles via detecting tiny signals from them, including atomic or optic clocks [53], optically pumped magnetometry [16–19], torsion balance [54,55], trapped ions [56,57], nitrogen-vacancy diamond [58], and other high-sensitivity techniques [59–66]. Searches for spin-dependent energy shifts caused by an anomalous interaction like a magnetic field are important methods. Various optical-magnetometry-based experiments [35,46,67] and worldwide coordinated searches, such as the global network of optical magnetometers for exotic (GNOME) physics searches [68], have been conducted to search for heretofore anomalous spin-dependent forces and particles and set constraints on them. Noble-gas spin amplification techniques have the intrinsic advantage of ultrahigh sensitivity, and most stringent constraints on axion-like dark matter and several exotic spin-dependent interactions are established [16–19].

The axion and other pseudoscalar bosons (collectively referred to as axion-like particles or ALPs), emerging with a global symmetry broken at ultrahigh energy scale, can be a solution to the strong-CP problem [69] and well-motivated dark matter candidates [70, 71]. ALPs can form a classical field $a \approx a_0 \cos(2\pi\nu_a t)$ oscillating at their Compton frequency $\nu_a = m_a \mathrm{c}^2/h$ [46,72–74], where m_a is the axion mass, c is the speed of light, and h is the Planck constant. The field amplitude a_0 can be estimated by the galactic dark-matter energy density $\rho_a = m_a^2 a_0^2 \mathrm{c}^2/(2\hbar^2) \approx 0.4\ \mathrm{GeV \cdot cm^{-3}}$ [70,75]. ALPs can interact with nuclear spins by a Zeeman-like Hamiltonian,

$$H_{\mathrm{int}} \approx \gamma \boldsymbol{B}_{\mathrm{ALP}} \cdot \boldsymbol{I}_{\mathrm{N}}, \tag{28}$$

where $\boldsymbol{B}_{\mathrm{ALP}} = g_{\mathrm{aNN}} \sqrt{2\hbar c \rho_a} \sin(2\pi\nu_a t) \boldsymbol{v}_a/\gamma$ represents the pseudomagnetic magnetic field induced by ALP dark matter [46,72] and $\boldsymbol{I}_{\mathrm{N}}$ is the nuclear spin operator. Here, g_{aNN} is the strength of the axion-nucleon coupling, with the definition used in [74] and the unit of GeV^{-1}. $|\boldsymbol{v}_a| \sim 10^{-3}\mathrm{c}$ represents the local galactic virial velocity [76], and γ is the gyromagnetic ratio of the nuclear spin. The core of the search scheme is to detect the pseudomagnetic field $\boldsymbol{B}_{\mathrm{ALP}}$ and constrain the strength g_{aNN} over some range of ALP masses.

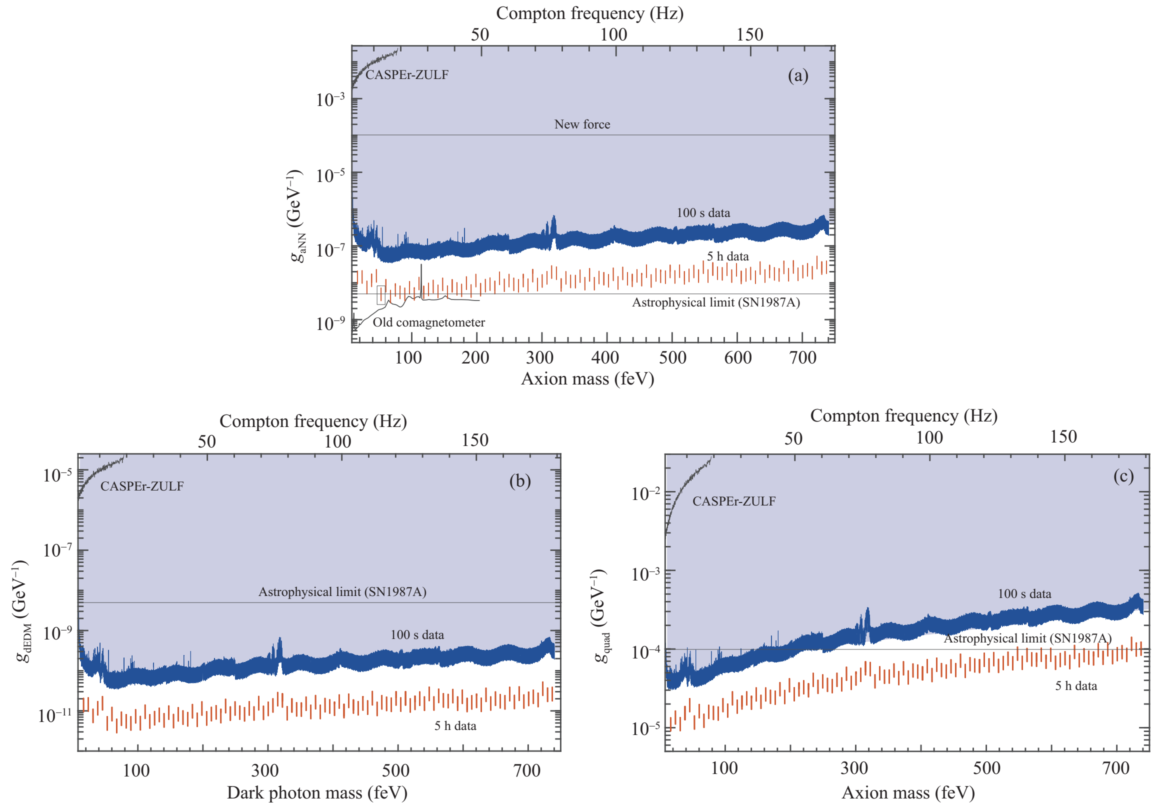

Figure 12 (Color online) Experimental results of searches for axion-like dark matter using the spin-amplifier-based magnetometer. (a) Limits on the axion-like dark matter-nucleon coupling g_{aNN}. The dark line shows the "Old comagnetometer" limits from [77]. (b) Limits on dark photon-nucleon coupling g_{dEDM}. (c) Limits on axion-like quadratic coupling with nucleon g_{quad}. The blue-shade is excluded by measurements (100 s for each run) and the red lines show the advanced sensitivity (5 h for each run). The grey line shows the limit given by the CASPEr-ZULF experiment [46]. The horizontal black lines show the laboratory searches for new spin-dependent forces and the astrophysical limit from supernova SN1987A cooling [78, 79]. Adapted and reprinted from [16].

The spin amplification technique has been demonstrated to search for ALP signals in the frequency range from 2 to 180 Hz, corresponding to the ALP mass range from 8.3 to 744 feV. The obtained limits overlap with the CASPEr-ZULF experiment for a mass range from 15 to 78 feV [46], improving previous limits by at least five orders of magnitude, as shown in Figure 12(a). A recent work [77] derived ALP limits below 200 feV based on the decade-old comagnetometer data from previously published work and could not access ALPs at higher Compton frequencies due to the sensitivity loss of comagnetometers [11]. In contrast, new limits are extended to unconstrained regions of the parameter space from 200 to 744 feV. Moreover, the spin amplification technique can also be used to constrain the quadratic interactions between axion-like particles and nucleons as well as interactions between dark photons and nucleons, exceeding bounds from astrophysical observations [78, 79], as shown in Figures 12(b) and (c).

Apart from searches for axionlike dark matter, the spin amplification technique has been used to search for exotic long-range spin-dependent interactions between fermions mediated by new light bosons [18, 19, 69, 80–83].

$$\begin{aligned}
V_{4+5} &= -f_{4+5}\frac{\hbar^2}{8\pi mc}[\hat{\boldsymbol{\sigma}}_1\cdot(\boldsymbol{v}\times\hat{r})]\left(\frac{1}{\lambda r}+\frac{1}{r^2}\right)\mathrm{e}^{-r/\lambda},\\
V_{12+13} &= f_{12+13}\frac{\hbar}{8\pi}(\hat{\boldsymbol{\sigma}}_1\cdot\boldsymbol{v})\left(\frac{1}{r}\right)\mathrm{e}^{-r/\lambda},\\
V_3 &= -\frac{f_3}{4\pi m_1 m_2}\left[(\hat{\boldsymbol{\sigma}}_1\cdot\hat{\boldsymbol{\sigma}}_2)\left(\frac{1}{\lambda r^2}+\frac{1}{r^3}\right)-(\hat{\boldsymbol{\sigma}}_1\cdot\hat{r})(\hat{\boldsymbol{\sigma}}_2\cdot\hat{r})\left(\frac{1}{\lambda^2 r}+\frac{3}{\lambda r^2}+\frac{3}{r^3}\right)\right]\mathrm{e}^{-r/\lambda},
\end{aligned}\tag{29}$$

where f_{4+5}, f_{12+13}, f_3 are dimensionless coupling constants, $\hat{\boldsymbol{\sigma}}_1$, $\hat{\boldsymbol{\sigma}}_2$ are the spin vectors and m_1, m_2 are the masses of the polarized fermions, $\boldsymbol{v}$ is the relative velocity between two interacting fermions, $\hat{r}$ is the unit vector in the direction between them, and $\lambda=\hbar(m_b c)^{-1}$ is the force range (or the boson Compton wavelength) with m_b being the light boson mass.

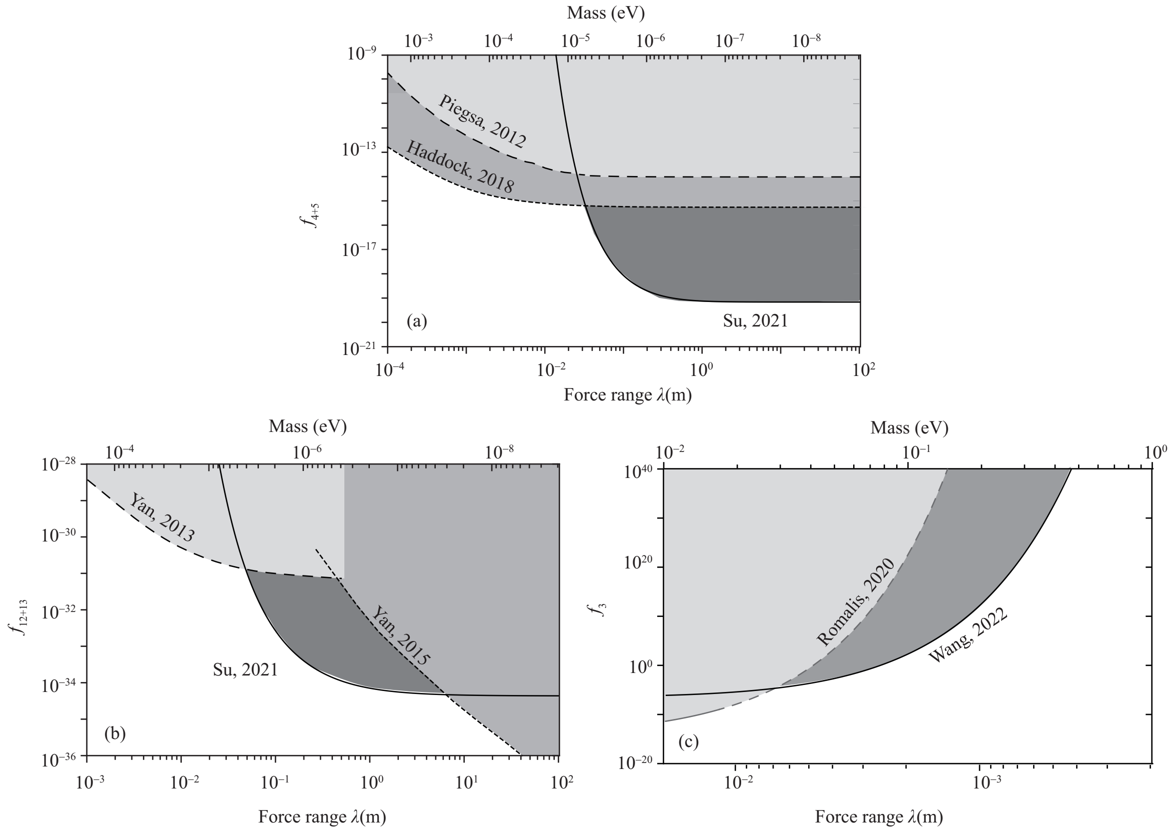

Figure 13 Experimental results of searches for exotic spin-dependent interactions using the spin-amplifier-based magnetometer. (a) Constraints on f_{4+5} (solid line, the most stringent constraints in the force range from 0.04 to 100 m [18]). The dashed lines represent bounds of f_{4+5} from [84, 85]. (b) Constraints on f_{12+13} (solid line, the most stringent constraints in the force range from 0.05 to 6 m). (c) Constraints on f_3 (solid line, the most stringent constraints in the force range from 0.0004 to 0.005 m). The thin gray curve indicates the same coupling derived from comagnetometer experiments [67], while the dashed one is deduced based on (29). Adapted and reprinted with permission from [18, 19] Copyright 2021 American Association for the Advancement of Science.

In principle, these interactions induce Zeeman-like energy shifts of ^{129}Xe spins [63],

$$-\boldsymbol{\mu}_{\mathrm{Xe}} \cdot \boldsymbol{B}_j^{\mathrm{exo}} = V_j, \tag{30}$$

where $\boldsymbol{\mu}_{\mathrm{Xe}}$ is the magnetic moment of ^{129}Xe spin, V_j represents the exotic spin-dependent potential $(V_2, V_3, \ldots, V_{16})$ and $\boldsymbol{B}_j^{\mathrm{exo}}$ is the corresponding pseudo-magnetic field. The pseudomagnetic fields of V_{4+5} and V_{12+13} are generated by a single rotating 112.34-g bismuth germanate insulator [$Bi_4Ge_3O_{12}$ (BGO)] crystal (mass source) in [18] and that of V_3 is produced by optically pumped ^{87}Rb electrons (spin source) in [19]. In general, the field $\boldsymbol{B}_j^{\mathrm{exo}}$ can be decomposed into

$$\boldsymbol{B}_j^{\mathrm{exo}} = \sum_N \boldsymbol{B}_N \cos(2\pi N\nu t + \phi_N), \tag{31}$$

where $N\nu$ is the frequency of the Nth harmonic, $\boldsymbol{B}_N$ is the Nth field, and ϕ_N is its phase. To maximize the exotic signal, the operation frequency of the spin-based amplifier is set at the frequency of the maximum harmonic. In this case, due to the relatively narrow bandwidth of the spin-based amplifier, only the signal of the dominant harmonic can be considerably amplified and the effect of other harmonics is negligible.

Figures 13(a) and (b) shows new constraints on f_{4+5} and f_{12+13} obtained in [18] with 95% confidence levels. The previous constraints on f_{4+5} were obtained with neutron experiments [84, 85]. In contrast, Ref. [18] set the most stringent constraints on f_{4+5} for the force range from 0.04 to 100 m and improved over previous constraints by about four orders of magnitude for $\lambda = 1.0$ m, as shown in Figure 13(a). In Figure 13(b), the most stringent constraints on f_{12+13} are obtained in the force range from 0.05 to 6 m. Previous studies established constraints with a cold neutron beam [86] ($\lambda < 0.06$ m) and with polarized ^{3}He [87] ($\lambda > 4$ m). Compared with them, the new constraints reach 1.01×10^{-34} at 0.45 m and improve over previous laboratory limits by at least two orders of magnitude. Figure 13(c) shows the new constraints on f_3 set in [19] together with recent constraint from experimental searches for exotic dipole-dipole interactions in 2020 [67]. For the mass range from 0.03 to 1 meV, the new result provides the most stringent constraint from direct measurements on f_3.

6 Conclusion and perspective

Quantum amplification that offers the capability of enhancing weak signals is ubiquitous and of central importance to various frontiers of science. Here we review recent progress on noble-gas spin amplification, which is realized through overlapping noble gas and alkali metal atoms with/without the periodically driven field. Combining the spin amplification and Floquet systems provides a powerful tool to build ultrasensitive quantum sensors, such as the spin-based amplifier, maser, Floquet spin amplifier, and Floquet maser. These sensors can achieve femtotesla sensitivity, which makes them attractive in magnetic-field sensing and searches for new physics beyond the standard model. It is worthy to emphasize that the periodically driven (Floquet) systems could become a promising platform to explore advanced quantum phenomena beyond ordinary systems and enable a variety of novel functionalities that might not be otherwise directly accessible, for example, time crystals [88], Floquet Raman transition [89], prethermalization [90], Floquet cavity electromagnonics [91], Floquet polaritons [92], and Floquet quantum detectors [93].

For now, the study of spin amplification is still in a very early stage and its future development is being faced with some potential challenges. In the spin amplification protocol, a central problem is how to realize the amplification factor as large as possible. Based on (14), the amplification factor η depends on three parameters of noble-gas spins: the polarization P_0^{n}, the maximum magnetization M_0^{n} determined by the atomic density and the coherence time $T_{2\mathrm{n}}$. The $\sim 10^7$ amplification factor can be in principle expected using ^{3}He-K systems due to the long coherence time of ^{3}He ($T_{2\mathrm{n}} > 1000$ s) [16,18,94]. However, it would be difficult to optimize these parameters to achieve the maximum amplification factor expected, since they are practically related to each other in a real experiment and determined by some very complicated mechanism. Besides, this technique also has some general technological limitations, such as magnetic noise, the leakage of noble gas, the fluctuation of the laser beam and the temperature. Finally, the spin amplification will also face some practical difficulties for diverse application scenarios, such as in an unshielded environment or in a moving vehicle. The trade-off between the amplification factor and the bandwidth may increase cost and power consumption in searching for a target signal.

In the future, we believe that the spin amplification techniques will progress dramatically over the coming years and shed new light on applications ranging from quantum metrology, investigation of the dynamics of the geomagnetic fields, and quantum information processing to fundamental physics.

Acknowledgements This work was supported by National Key Research and Development Program of China (Grant No. 2018YFA0306600), National Natural Science Foundation of China (Grant Nos. 11661161018, 11927811, 12004371), Anhui Initiative in Quantum Information Technologies (Grant No. AHY050000), and USTC Research Funds of the Double First-Class Initiative (Grant No. YD3540002002).

References

1 Estermann I, Frisch R, Stern O. Magnetic moment of the proton. Nature, 1933, 132: 169–170
2 Walker T G, Happer W. Spin-exchange optical pumping of noble-gas nuclei. Rev Mod Phys, 1997, 69: 629–642
3 Albert M S, Cates G D, Driehuys B, et al. Biological magnetic resonance imaging using laser-polarized ^{129}Xe. Nature, 1994, 370: 199–201
4 Wu Z. Wall interactions of spin-polarized atoms. Rev Mod Phys, 2021, 93: 035006
5 Gentile T R, Nacher P J, Saam B, et al. Optically polarized ^{3}He. Rev Mod Phys, 2017, 89: 045004
6 Schaefer S R, Cates G D, Chien T R, et al. Frequency shifts of the magnetic-resonance spectrum of mixtures of nuclear spin-polarized noble gases and vapors of spin-polarized alkali-metal atoms. Phys Rev A, 1989, 39: 5613–5623
7 Gross S, Barmet C, Dietrich B E, et al. Dynamic nuclear magnetic resonance field sensing with part-per-trillion resolution. Nat Commun, 2016, 7: 1–7
8 Wu T, Blanchard J W, Kimball D F J, et al. Nuclear-spin comagnetometer based on a liquid of identical molecules. Phys Rev Lett, 2018, 121: 023202
9 Farooq M, Chupp T, Grange J, et al. Absolute magnetometry with ^{3}He. Phys Rev Lett, 2020, 124: 223001
10 Jiménez-Martínez R, Kennedy D J, Rosenbluh M, et al. Optical hyperpolarization and NMR detection of ^{129}Xe on a microfluidic chip. Nat Commun, 2014, 5: 3908
11 Kornack T W, Ghosh R K, Romalis M V. Nuclear spin gyroscope based on an atomic comagnetometer. Phys Rev Lett, 2005, 95: 230801
12 Chupp T E, Oteiza E R, Richardson J M, et al. Precision frequency measurements with polarized ^{3}He, ^{21}Ne, and ^{129}Xe atoms. Phys Rev A, 1988, 38: 3998–4003
13 Giovannetti V, Lloyd S, Maccone L. Quantum-enhanced measurements: beating the standard quantum limit. Science, 2004, 306: 1330–1336

14 Giovannetti V, Lloyd S, Maccone L. Advances in quantum metrology. Nat Photon, 2011, 5: 222–229
15 Pezzé L, Smerzi A, Oberthaler M K, et al. Quantum metrology with nonclassical states of atomic ensembles. Rev Mod Phys, 2018, 90: 035005
16 Jiang M, Su H, Garcon A, et al. Search for axion-like dark matter with spin-based amplifiers. Nat Phys, 2021, 17: 1402–1407
17 Jiang M, Su H, Wu Z, et al. Floquet maser. Sci Adv, 2021, 7: eabe0719
18 Su H, Wang Y, Jiang M, et al. Search for exotic spin-dependent interactions with a spin-based amplifier. Sci Adv, 2021, 7: eabi9535
19 Wang Y, Su H, Jiang M, et al. Limits on axions and axionlike particles within the axion window using a spin-based amplifier. ArXiv:2201.11847, 2022
20 DeMille D, Doyle J M, Sushkov A O. Probing the frontiers of particle physics with tabletop-scale experiments. Science, 2017, 357: 990–994
21 Safronova M S, Budker D, DeMille D, et al. Search for new physics with atoms and molecules. Rev Mod Phys, 2018, 90: 025008
22 Budker D, Graham P W, Ledbetter M, et al. Proposal for a cosmic axion spin precession experiment (CASPEr). Phys Rev X, 2014, 4: 021030
23 Arvanitaki A, Geraci A A. Resonantly detecting axion-mediated forces with nuclear magnetic resonance. Phys Rev Lett, 2014, 113: 161801
24 Jiang M, Qin Y, Wang X, et al. Floquet spin amplification. Phys Rev Lett, 2022, 128: 233201
25 Wu Z K, Kitano M, Happer W, et al. Optical determination of alkali metal vapor number density using Faraday rotation. Appl Opt, 1986, 25: 4483–4492
26 Opechowski W. Magneto-optical effects and paramagnetic resonance. Rev Mod Phys, 1953, 25: 264–268
27 Jiang M, Xu W, Li Q, et al. Interference in atomic magnetometry. Adv Quantum Tech, 2020, 3: 2000078
28 Moessner R, Sondhi S L. Equilibration and order in quantum Floquet matter. Nat Phys, 2017, 13: 424–428
29 Eckardt A. Colloquium: atomic quantum gases in periodically driven optical lattices. Rev Mod Phys, 2017, 89: 011004
30 Shirley J H. Solution of the Schrödinger equation with a Hamiltonian periodic in time. Phys Rev, 1965, 138: 979–987
31 Jin L, Pfender M, Aslam N, et al. Proposal for a room-temperature diamond maser. Nat Commun, 2015, 6: 8251
32 Oxborrow M, Breeze J D, Alford N M. Room-temperature solid-state maser. Nature, 2012, 488: 353–356
33 Suefke M, Lehmkuhl S, Liebisch A, et al. Para-hydrogen raser delivers sub-millihertz resolution in nuclear magnetic resonance. Nat Phys, 2017, 13: 568–572
34 Kotler S, Akerman N, Glickman Y, et al. Single-ion quantum lock-in amplifier. Nature, 2011, 473: 61–65
35 Aggarwal N, Schnabel A, Voigt J, et al. Characterization of magnetic field noise in the ARIADNE source mass rotor. 2020. ArXiv:2011.12617
36 Kraus H, Soltamov V A, Riedel D, et al. Room-temperature quantum microwave emitters based on spin defects in silicon carbide. Nat Phys, 2014, 10: 157–162
37 Breeze J D, Salvadori E, Sathian J, et al. Continuous-wave room-temperature diamond maser. Nature, 2018, 555: 493–496
38 Gordon J P, Zeiger H J, Townes C H. The maser—new type of microwave amplifier, frequency standard, and spectrometer. Phys Rev, 1955, 99: 1264–1274
39 Goldenberg H M, Kleppner D, Ramsey N F. Atomic hydrogen maser. Phys Rev Lett, 1960, 5: 361–362
40 Bienfait A, Pla J J, Kubo Y, et al. Controlling spin relaxation with a cavity. Nature, 2016, 531: 74–77
41 Bloembergen N, Pound R V. Radiation damping in magnetic resonance experiments. Phys Rev, 1954, 95: 8–12
42 Sato T, Ichikawa Y, Kojima S, et al. Development of co-located ^{129}Xe and ^{131}Xe nuclear spin masers with external feedback scheme. Phys Lett A, 2018, 382: 588–594
43 Gordon J P, Zeiger H J, Townes C H. The maser—new type of microwave amplifier, frequency standard, and spectrometer. Phys Rev, 1955, 99: 1264–1274
44 Marfaing J, Bois J J, Blancon R, et al. About the world-wide magnetic-background noise in the millihertz frequency range. Europhys Lett, 2009, 88: 19002
45 Wu T, Blanchard J W, Centers G P, et al. Search for axionlike dark matter with a liquid-state nuclear spin comagnetometer. Phys Rev Lett, 2019, 122: 191302
46 Garcon A, Blanchard J W, Centers G P, et al. Constraints on bosonic dark matter from ultralow-field nuclear magnetic resonance. Sci Adv, 2019, 5: eaax4539
47 Shah V, Knappe S, Schwindt P D D, et al. Subpicotesla atomic magnetometry with a microfabricated vapour cell. Nat Photon, 2007, 1: 649–652
48 Boto E, Holmes N, Leggett J, et al. Moving magnetoencephalography towards real-world applications with a wearable system. Nature, 2018, 555: 657–661
49 Budker D, Romalis M. Optical magnetometry. Nat Phys, 2007, 3: 227–234
50 Budker D, Gawlik W, Kimball D F, et al. Resonant nonlinear magneto-optical effects in atoms. Rev Mod Phys, 2002, 74: 1153–1201
51 Allred J C, Lyman R N, Kornack T W, et al. High-sensitivity atomic magnetometer unaffected by spin-exchange relaxation. Phys Rev Lett, 2002, 89: 130801
52 Kominis I K, Kornack T W, Allred J C, et al. A subfemtotesla multichannel atomic magnetometer. Nature, 2003, 422: 596–599
53 Derevianko A, Pospelov M. Hunting for topological dark matter with atomic clocks. Nat Phys, 2014, 10: 933–936
54 Terrano W A, Adelberger E G, Lee J G, et al. Short-range, spin-dependent interactions of electrons: a probe for exotic pseudo-goldstone bosons. Phys Rev Lett, 2015, 115: 201801
55 Ding J, Wang J, Zhou X, et al. Constraints on the velocity and spin dependent exotic interaction at the micrometer range. Phys Rev Lett, 2020, 124: 161801
56 Wineland D J, Bollinger J J, Heinzen D J, et al. Search for anomalous spin-dependent forces using stored-ion spectroscopy. Phys Rev Lett, 1991, 67: 1735–1738
57 Kotler S, Ozeri R, Kimball D F J. Constraints on exotic dipole-dipole couplings between electrons at the micrometer scale. Phys Rev Lett, 2015, 115: 081801
58 Rong X, Wang M, Geng J, et al. Searching for an exotic spin-dependent interaction with a single electron-spin quantum sensor. Nat Commun, 2018, 9: 1–7
59 Bulatowicz M, Griffith R, Larsen M, et al. Laboratory search for a long-range T-odd P-odd interaction from axionlike particles using dual-species nuclear magnetic resonance with polarized ^{129}Xe and ^{131}Xe gas. Phys Rev Lett, 2013, 111: 102001

60 Tullney K, Allmendinger F, Burghoff M, et al. Constraints on spin-dependent short-range interaction between nucleons. Phys Rev Lett, 2013, 111: 100801

61 Ficek F, Kimball D F J, Kozlov M G, et al. Constraints on exotic spin-dependent interactions between electrons from helium fine-structure spectroscopy. Phys Rev A, 2017, 95: 032505

62 Ficek F, Fadeev P, Flambaum V V, et al. Constraints on exotic spin-dependent interactions between matter and antimatter from antiprotonic helium spectroscopy. Phys Rev Lett, 2018, 120: 183002

63 Ni W T, Pan S S, Yeh H C, et al. Search for an axionlike spin coupling using a paramagnetic salt with a dc SQUID. Phys Rev Lett, 1999, 82: 2439–2442

64 Kimball D F J, Boyd A, Budker D. Constraints on anomalous spin-spin interactions from spin-exchange collisions. Phys Rev A, 2010, 82: 062714

65 Stadnik Y V, Dzuba V A, Flambaum V V. Improved limits on axionlike-particle-mediated P, T-violating interactions between electrons and nucleons from electric dipole moments of atoms and molecules. Phys Rev Lett, 2018, 120: 013202

66 Dzuba V A, Flambaum V V, Samsonov I B, et al. New constraints on axion-mediated P, T-violating interaction from electric dipole moments of diamagnetic atoms. Phys Rev D, 2018, 98: 035048

67 Almasi A, Lee J, Winarto H, et al. New limits on anomalous spin-spin interactions. Phys Rev Lett, 2020, 125: 201802

68 Afach S, Buchler B C, Budker D, et al. Search for topological defect dark matter with a global network of optical magnetometers. Nat Phys, 2021, 17: 1396–1401

69 Peccei R D, Quinn H R. CP conservation in the presence of pseudoparticles. Phys Rev Lett, 1977, 38: 1440–1443

70 Preskill J, Wise M B, Wilczek F. Cosmology of the invisible axion. Phys Lett B, 1983, 120: 127–132

71 Kim J E, Carosi G. Axions and the strong CP problem. Rev Mod Phys, 2010, 82: 557–601

72 Smorra C, Stadnik Y V, Blessing P E, et al. Direct limits on the interaction of antiprotons with axion-like dark matter. Nature, 2019, 575: 310–314

73 Graham P W, Kaplan D E, Mardon J, et al. Spin precession experiments for light axionic dark matter. Phys Rev D, 2018, 97: 055006

74 Graham P W, Rajendran S. New observables for direct detection of axion dark matter. Phys Rev D, 2013, 88: 035023

75 Dine M, Fischler W. The not-so-harmless axion. Phys Lett B, 1983, 120: 137–141

76 Kimball D F J, Afach S, Aybas D, et al. Overview of the cosmic axion spin precession experiment (CASPEr). In: Proceedings of Microwave Cavities and Detectors for Axion Research, 2020. 105–121

77 Bloch I M, Hochberg Y, Kuflik E, et al. Axion-like relics: new constraints from old comagnetometer data. J High Energ Phys, 2020, 2020: 167

78 Vysotsskii M, Zel'Dovich Y B, Khlopov M Y, et al. Some astrophysical limitations on the axion mass. J Exp Theor Phys Lett, 1978, 27: 533

79 Raffelt G G. Astrophysical axion bounds. In: Proceedings of Axions, 2008. 51–71

80 Ramsey N F. The tensor force between two protons at long range. Phys A-Stat Mech Its Appl, 1979, 96: 285–289

81 Wilczek F. Problem of strong P and T invariance in the presence of instantons. Phys Rev Lett, 1978, 40: 279–282

82 Weinberg S. A new light boson? Phys Rev Lett, 1978, 40: 223–226

83 Fadeev P, Stadnik Y V, Ficek F, et al. Revisiting spin-dependent forces mediated by new bosons: potentials in the coordinate-space representation for macroscopic- and atomic-scale experiments. Phys Rev A, 2019, 99: 022113

84 Piegsa F M, Pignol G. Limits on the axial coupling constant of new light bosons. Phys Rev Lett, 2012, 108: 181801

85 Haddock C, Amadio J, Anderson E, et al. A search for possible long range spin dependent interactions of the neutron from exotic vector boson exchange. Phys Lett B, 2018, 783: 227–233

86 Yan H, Snow W M. New limit on possible long-range parity-odd interactions of the neutron from neutron-spin rotation in liquid ^{4}He. Phys Rev Lett, 2013, 110: 082003

87 Yan H, Sun G A, Peng S M, et al. Searching for new spin- and velocity-dependent interactions by spin relaxation of polarized ^{3}He Gas. Phys Rev Lett, 2015, 115: 182001

88 Else D V, Bauer B, Nayak C. Floquet time crystals. Phys Rev Lett, 2016, 117: 090402

89 Shu Z, Liu Y, Cao Q, et al. Observation of Floquet Raman transition in a driven solid-state spin system. Phys Rev Lett, 2018, 121: 210501

90 Peng P, Yin C, Huang X, et al. Floquet prethermalization in dipolar spin chains. Nat Phys, 2021, 17: 444–447

91 Xu J, Zhong C, Han X, et al. Floquet cavity electromagnonics. Phys Rev Lett, 2020, 125: 237201

92 Clark L W, Jia N, Schine N, et al. Interacting Floquet polaritons. Nature, 2019, 571: 532–536

93 Bloch I M, Ronen G, Shaham R, et al. New constraints on axion-like dark matter using a Floquet quantum detector. Sci Adv, 2022, 8: eabl8919

94 Ma J X, Lan Y, Yan H Y. Experimental design and optimization of resonantly searching for exotic axion-like particles. Sci Sin-Phys Mech Astron, 2022